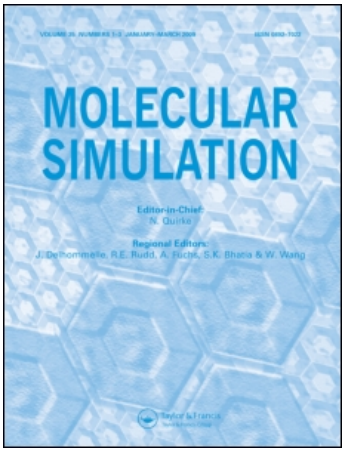

Molecular Simulation
Publication details, including instructions for authors and subscription information:
http://www.informaworld.com/smpp/title~content=t713644482

Simulation Studies of a Lennard-Jones Liquid in Micropores

J. M. D. Macelroy[a]; S. -H. Suh[b]
[a] Chemical Engineering Department, University of Missouri-Rolla, Rolla, Missouri, U. S. A. [b] Department of Chemistry, University of Lethbridge, Lethbridge, Canada

To cite this Article Macelroy, J. M. D. and Suh, S. -H.(1989) 'Simulation Studies of a Lennard-Jones Liquid in Micropores', Molecular Simulation, 2: 4, 313 — 351
To link to this Article: DOI: 10.1080/08927028908034609
URL: http://dx.doi.org/10.1080/08927028908034609

Molecular Simulation, 1989, Vol. 2, pp. 313–351
Reprints available directly from the publisher
Photocopying permitted by license only

SIMULATION STUDIES OF A LENNARD-JONES LIQUID IN MICROPORES†

J.M.D. MACELROY

Chemical Engineering Department, University of Missouri-Rolla, Rolla, Missouri 65401, U.S.A.

S.-H. SUH

Department of Chemistry, University of Lethbridge, Lethbridge, Alberta T1K 3M4 Canada

(*Received March 1988, in final form May 1988*)

In this paper grand canonical ensemble Monte Carlo and molecular dynamics simulation techniques are used to establish the degree to which the equilibrium and transport properties of fluids in micropores are influenced both by confinement in the narrow pore space and by the lattice structure of the pore wall. Partition coefficients, solvation forces, and diffusion coefficients for a Lennard-Jones liquid confined within two model cylindrical pores are determined over a range of effective micropore sizes. In one model the cylindrical pore wall is described by a structureless, continuum interaction potential similar to that which is frequently employed in theoretical studies of adsorption. In the second model a single embedded layer of lattice atoms is placed at the solid/fluid interface.

The results obtained are compared with the prediction of a bulk fluid approximation and the Fischer-Methfessel approximation to the Yvon-Born-Green equation and the recently developed kinetic theory of Davis for micropore fluids. These theories are shown to agree very favorably with the simulation results for the structureless model although quantitatively less so for pores with structured walls.

KEY WORDS: Micropores, Lennard-Jones fluid, density profiles, solvation forces, diffusion

1. INTRODUCTION

The chemical and biochemical process industries currently employ a wide variety of microporous materials either in heterogeneous catalysis or for separating multicomponent mixtures. In a few cases the pores of these materials have a well-defined geometry (for example zeolites) however in many situations the internal pore structure is complicated and pore shape idealizations such as the slit, cylindrical, or spherical cavity have been used. Whichever model one assumes as a description of the pore space, a feature which they share in common as micropore structures is the hindrance offered to the molecules of the pore fluid due to the proximity of the pore walls.

Recent developments towards an improved understanding of the equilibrium properties of confined fluids and liquids have included both theoretical and computational methods in statistical mechanics [1–13]. The most widely studied pore geometries have been the slit and cylindrical models and the results reported to date have shed light on a number of molecular phenomena underlying experimental observations. In particular we mention the qualitative agreement between the solvation force measurements of Israelachvili and coworkers [14, 15] and Christenson [16] and

† Invited paper.

computer simulations of Lennard-Jones fluids in slit-shaped pores [2,3,6,7,11]. These oscillatory forces are intimately related to molecular size effects in very fine pores and, with the aid of current theoretical methods for calculating fluid density profiles, they may now be predicted with reasonable accuracy for simple systems [9].

The influence of molecular size-exclusion on the transport properties of dense fluids and liquids in micropores has also received considerable attention although up until recently the interpretation of the mechanisms involved has been largely based on hydrodynamic concepts [17–19]. One of the major consequences of molecular size-exclusion in very fine, liquid-filled pores is a severe reduction in solute diffusional transport rates and, in order to compute the diffusion flux for nonadsorbing solutes, hydrodynamic or empirical models [20–22] only require a knowledge of the solute particle reduced radius $\lambda = R/R_p$, where R_p is the average cylindrical pore radius. In a recent paper Davis [23] has proposed an alternative approach using an approximate kinetic theory for inhomogeneous fluids and in a subsequent publication [24] this theory was shown to be in very good agreement with molecular dynamics simulation results for a Lennard-Jones fluid confined within a slit-shaped pore. A similar analysis has not yet been considered for the cylindrical pore model nor has a comparison with available experimental data been made.

In this paper we report grand canonical ensemble Monte Carlo (GCEMC) and molecular dynamics (MD) simulation results for a single component Lennard-Jones (12–6) liquid in cylindrical micropores. The state point for the bulk liquid was chosen to be $(n_B^*, T^*) = (0.608, 1.15)$ where n_B^* is the bulk fluid number density reduced by σ^{-3}, T^* is the reduced temperature kT/ε, and σ and ε are the characteristic particle diameter and potential well depth appearing in the Lennard-Jones potential energy function. Two pore models are examined, one of which has a smooth structureless solid surface and a second model which has a surface structure similar to that of a simple cubic crystal of Lennard-Jones particles.

The motivation for investigating the properties of a micropore fluid in contact with two different solid surfaces is provided by our previous studies of hard-sphere fluids [25, 26] and by contrasts observed with empirical correlations for diffusion in microporous media [20–22]. In [25] we reported molecular dynamics simulation results for tracer self-diffusion in cylindrical pores with specularly reflecting and diffusely reflecting smooth walls. The diffusion coefficients obtained from the specular scattering studies were similar in magnitude to the corresponding bulk values and this is inconsistent with experimental observations. Here we will show that a similar situation can arise for a realistic fluid in a continuum cylindrical pore unless some measure of backscattering is introduced. Diffuse reflection on its own however will not fully account for the disparity between theory and experiment since the self-diffusion and binary diffusion coefficients reported in [25] and [26] respectively for this mode of scattering were still somewhat larger than the experimental results by a factor of two or more. Typical pore dimensions in microporous solids are such that between one and ten liquid layers may coexist with a bulk liquid phase of similar density and therefore the topology of the pore space and/or the structure of the solid surface will play an important role. The second of these effects is considered here using the structured surface model mentioned above.

In the next section we will describe the pore models investigated in this work and the equations used to analyze the simulation data. Technical details of the simulation methods employed are outlined in the appendix. The results obtained include density profiles, partition coefficients, and solvation forces as well as diffusion coefficients.

and are discussed in Section 3. For comparative purposes we also report theoretical results predicted by two approximations to the Yvon-Born-Green (YBG) equation [1,4,10] and the modified Enskog kinetic theory proposed by Davis [23]. Finally, in Section 4 we will summarize the most important aspects of our results and present our conclusions.

2. PORE MODELS AND THEORETICAL BACKGROUND.

The two pore models employed in this work are illustrated schematically in Figure 1. The fluid particle/pore wall potential interaction for wall 1 is described by [27]

$$\phi_{iW}^{(1)}(R_P - r_i) = \frac{2\pi}{3}\varepsilon_{iW} n_W \sigma_{iW}^3 \left[\frac{2}{15}\left(\frac{\sigma_{iW}}{R_P - r_i}\right)^9 f^{(9)}(r_i) - \left(\frac{\sigma_{iW}}{R_P - r_i}\right)^3 f^{(3)}(r_i)\right] \quad (1)$$

where $f^{(9)}(r_i)$ and $f^{(3)}(r_i)$ are 10th order polynomials in the radial coordinate r_i of particle i and R_P is the radius of the cylinder which passes through the centers of the surface wall particles. Equation (1) is based on the assumption that the solid wall behaves as a continuum.

In the potential model for wall 2 we relax the assumption of continuum interactions with the first layer of wall particles. In this case

$$\phi_{iW}^{(2)}(r_{iW}) = \phi_{iW}^{(1)}\left(R_P + \frac{\sigma_{iW}}{2} - r_i\right) + \sum_{j\in S} 4\varepsilon_{iW}\left[\left(\frac{\sigma_{iW}}{r_{ij}}\right)^{12} - \left(\frac{\sigma_{iW}}{r_{ij}}\right)^6\right](1 - U(r_{ij} - R_c)) \quad (2)$$

The last term in this equation represents pairwise additive London-van der Waals interactions between particle i in the pore fluid and a periodic layer of surface atoms $\{S\}$ located at a radial distance R_P from the center of the pore. The step function $U(r_{ij} - R_c)$ designates truncation of the ij pair interaction at the cut-off radius R_c (in our case $R_c = 3.3\sigma$) and the coordinates of the surface atoms are simply expressed as

$$\boldsymbol{r}_j(j\in S) = R_P\cos\left(\frac{2\pi k}{N_R}\right)\boldsymbol{i}_x + R_P\sin\left(\frac{2\pi k}{N_R}\right)\boldsymbol{i}_y + \sigma_w l\boldsymbol{i}_z$$
$$(k = 1, \ldots, N_R;\quad l = -\infty, \ldots, +\infty) \quad (3)$$

where N_R is the number of surface atoms in a polygonal ring ($N_R = 12$ for the diagram shown in Figure 1(b)). σ_W in Equation (3) is the axial lattice spacing of the polygonal rings.

The pair potential for fluid particle interactions is given by

$$\phi_{ij}(r_{ij}) = 4\varepsilon\left[\left(\frac{\sigma}{r_{ij}}\right)^{12} - \left(\frac{\sigma}{r_{ij}}\right)^6\right](1 - U(r_{ij} - R_c)) \quad (4)$$

where R_c is the cut-off radius defined with Equation (2).

In all of the pore simulations conducted here we chose $\varepsilon_{iW} = \varepsilon$ and we set the Lennard-Jones diameter σ_{iW} and the lattice spacing σ_W equal to σ. All relevant length scales were reduced by this quantity. The dimensionless number density $n_W\sigma_{iW}^3$ in Equation (1) was also taken to be equal to 1.0 which, for a planar wall, corresponds

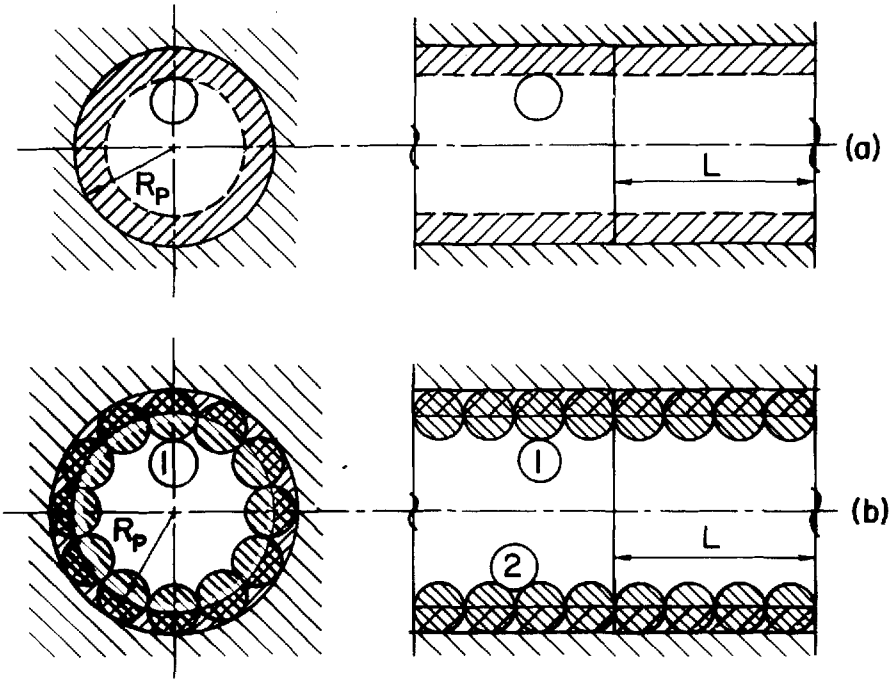

Figure 1 Model cylindrical pore structures. (a) Wall 1: particle/pore wall continuum interactions. The hatched region $r < R_p$ represents the inner repulsion core of the solid surface atoms. (b) Wall 2: particle/pore wall non-continuum interactions. Axial positions 1 and 2 are referred to as the pore window and polygonal cage respectively.

to a simple cubic lattice with a cell spacing equal to σ (i.e. the analogue of a solid with surface atoms located in accord with Equation (3)). Furthermore, we note that in Equation (2) we have placed the background continuum potential at $R_p + (\sigma/2)$ rather than at $R_p + \sigma$ and the reason for this is explained with reference to Figure 2(a). In this figure we plot Equations (1) and (2) reduced by kT for a semi-infinite planar solid ($N_R = \infty$, $R_p = \infty$). By placing the background potential $\phi_W^{(1)}$ at $R_p + (\sigma/2)$ it may be shown that the potential curves for the structured surface at the three locations indicated in Figure 2(a) essentially coincide, within the thickness of the drawn lines, with the corresponding results for an untruncated semi-infinite simple cubic crystal. The maximum difference between Equation (2) and the full crystal interaction is approximately 2% and the disparity is only 0.5% or less at the potential minima. The rather large discrepancy between the continuum and crystal interaction is typical of the (9–3) integrated potential [28] and to emphasize how this difference can influence the properties of the pore fluid we have not attempted to adjust any of the parameters in Equation (1). (The analogy with a simple cubic crystal is, of course, imprecise for curved cylindrical surfaces, however for the purposes of this paper we may view Equations (1) and (2) as qualitative descriptions of different extremes of the same solid material).

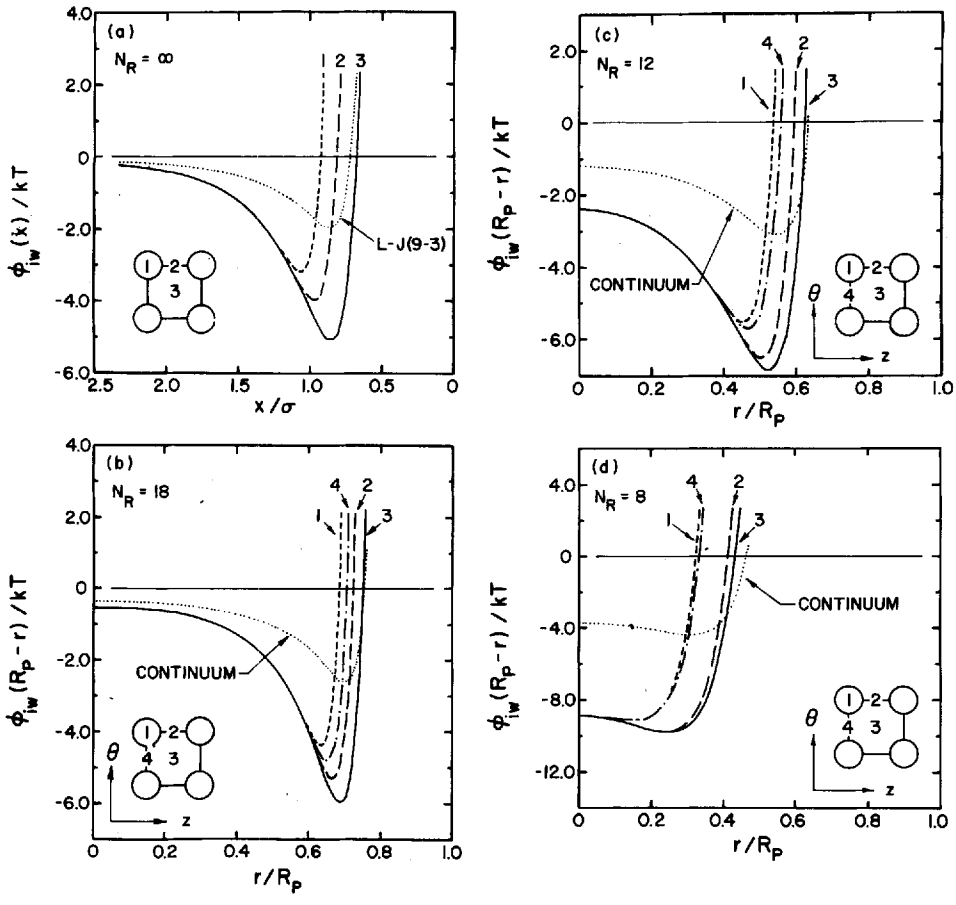

Figure 2 Particle/pore wall interaction potentials for different pores sizes with the Lennard-Jones particle at selected positions over the solid surface (a unit cell of the structured surface is schematically represented by the inset). · · · · · Structureless pore wall (Equation (1)): The selected positions over the structured pore wall (Equation (2)) are as follows: – – – – 1 over a surface atom, — — — 2 over a saddle point in the axial (z) direction, ——— 3 over an adsorption site, –·–·– 4 over a saddle point in the tangential (θ) direction. (a) Semi-infinite planar solid; (b) cylindrical pore with $N_R = 18$ ($R_p^* = 2.879$); (c) $N_R = 12$ ($R_p^* = 1.932$); (d) $N_R = 8$ ($R_p^* = 1.307$).

In Figures 2(b) through 2(d) we plot the potential functions for three representative pores sizes ($R_p = \sigma/(2 \sin(\pi/N_R))$). Apart from the distinction between the continuum and structured models there are two features worth noting in the potentials given by Equation (2). Due to the curvature of the pore wall the saddle point at position 4 has a shallower minimum than the axial saddle point at position 2. As the pore size decreases the potential curves at locations 1 and 4 approach one another and the same is seen to occur for the potentials at locations 2 and 3. For $N_R = 8$ the interactions within the polygonal cage and in the pore window (Figure 1(b)) are largely independent of θ and this result is analogous to the idealized sinusoidal potential function sometimes used to describe the potential energy surface in zeolite pores [29].

The second feature which we observe from Figure 2 is the relatively small energy barrier ($\sim kT$) for motion of an isolated Lennard-Jones particle in the axial direction of the pore. We will later show that this small degree of nonuniformity is sufficient to lead to highly structured density profiles and very low diffusion coefficients in liquid-filled pores.

The equilibrium properties computed in the simulations were the density profiles, partition coefficients and solvation forces. For structureless pore walls (Equation (1)) the fluid density only varies in the radial direction of the pore and profiles were calculated by dividing the pore cross-section up into equal increments of 0.01 R_P^* where R_P^* is in units of σ. For pores represented by Equation (2) the fluid density varies with r, z and θ and to avoid significant statistical sampling errors which could be incurred with too fine a grid spacing, we have computed profiles with a radial spacing of 0.01 R_P^*, an axial spacing of 0.1 (σ units), and an angular spacing of $0.2\pi/N_R$. Owing to the periodic symmetry of the structured pore this grid arrangement provides sufficiently accurate density profiles for our purposes. As will be discussed later, these profiles are employed as input data files in the analysis of the YBG equation [1,4,10] and Davis' kinetic theory for micropore fluids [23], however in Section 3 we will present angle averaged profiles at selected positions with the pores. In addition, we will also provide z as well as θ averaged radial profiles for comparison with the profiles obtained for the structureless pore model.

The equilibrium partition coefficient for a fluid distributing between a bulk phase and a pore is simply defined as

$$K = \frac{1}{V_P n_B} \int_{V_P} \langle n_P(\boldsymbol{r}) \rangle \, d\boldsymbol{r}$$

$$= \frac{\langle n_P \rangle}{n_B} \tag{5}$$

where $\langle n_P(\boldsymbol{r}) \rangle$ and $\langle n_P \rangle$ are the local and volume averaged number densities of the fluid in the pore respectively and V_P is the pore volume.

In order to compute K using Equation (5) and to define a characteristic pore radius for the models shown in Figure 1 we have employed the following dividing-surface concept. For the axisymmetric and axially invariant potential model given in Equation (1) the density profile of the pore fluid in the low density limit is

$$\frac{n_P(r)}{n_B} = \exp\left(- \frac{\phi_w^{(1)}(R_p - r)}{kT} \right) \tag{6}$$

At a particular radial position r_M near the pore wall $n_P(r)$ passes through a maximum and rapidly decays to zero as r approaches R_P. In the range $r_M < r < R_P$ we define a dividing surface at $r = R$ such that

$$\int_{r_M}^{R} (n_P(r_M) - n_P(r)) \, r \, dr = \int_{R}^{R_P} (n_P(r) - n_P(R_P)) \, r \, dr \tag{7}$$

Using Equation (6) and noting that $n_P(R_P) = 0$ then

$$R = \sqrt{r_M^2 + 2I} \tag{8}$$

where

$$I = \int_{r_M}^{R_P} \exp\left(- \frac{\phi_W^{(1)}(R_P - r)}{kT} \right) r \, dr \tag{9}$$

The effective pore radius is now defined to be

$$R^*_{PEFF} = R^* + 1/2 \tag{10}$$

where R^*_{PEFF} and R^* are in units of σ.

For wall 2 (Equation (2)) we have also employed the above procedure to obtain R^*_{PEFF}. In this case $\phi^{(1)}_W (R_P - r)$ in Equation (9) is replaced by a "Boltzmann-averaged" potential $\phi^{(2)}_{WB} (R_P - r)$ defined in a manner similar to that proposed by Abraham [30]

$$\exp\left(- \frac{\phi^{(2)}_{WB} (R_P - r)}{kT} \right) = \frac{1}{4\pi L} \int_{-L}^{L} \int_0^{2\pi} \exp\left(- \frac{\phi^{(2)}_w (r_{iw})}{kT} \right) d\theta dz \tag{11}$$

where, in principle, the limits $\pm L$ to extend to $\pm \infty$. These limits are, however, only needed for the second term in Equation (2) and the cut-off radius R_c simplifies the evaluation of this integral.

The radii R^*_{PEFF} were calculated at a reduced temperature $T^* = 1.15$ and these values were used to determine the particle reduced radius λ. Our primary reason for defining λ in this manner is that it provides a convenient basis for comparing the results obtained here for a Lennard-Jones fluid with those reported in [25, 31] for a hard-sphere fluid at a bulk density $n^*_B = 0.6$. It is also worth noting that Equations (8) – (10) give the precise definition of the pore radius for hard-sphere fluids in pores with hard walls ($\phi_W = 0$ for $r < r_M$, $\phi_W = \infty$ for $r \geqslant r_M$).

The remaining equilibrium property of interest here is the solvation force exerted by the fluid particles on the pore wall. For the structureless model the force normal to the pore wall is calculated using Equation (1) (i.e. in common with earlier studies of the solvation force in slit-shaped continuum pores [2,3,6,7,11], we treat Equation (1) as a two-body potential). The solvation force per unit area of the cylindrical surface at $r = R_P$ is then given by

$$f_s = - \frac{1}{4\pi R_P L} \left\langle \sum_{i=1}^{N} \frac{d\phi^{(1)}_{iW}}{dr_{iW}} \right\rangle \tag{12a}$$

$$= \frac{1}{4\pi R_P L} \int_{V_P} n_P(\boldsymbol{r}) \frac{d\phi^{(1)}_W}{dr} \, d\boldsymbol{r} \tag{12b}$$

where L is the half-length of the periodic pore and N is the total number of fluid particles employed in a given simulation.

The solvation force for wall 2 is similarly defined however in this case the radial forces acting on the surface atoms of the pore wall are individually summed.

$$f_s = - \frac{1}{4\pi r_P L} \left\langle \sum_{i=1}^{N} \left[\frac{d\phi^{(1)}_{iW}}{dr_{iW}} + \sum_{j \in S} \frac{\boldsymbol{r}_j \cdot \boldsymbol{r}_{ij}}{r_j \, r_{ij}} \frac{d\phi_{ij}}{dr_{ij}} \right] \right\rangle \tag{13a}$$

$$= \frac{1}{4\pi R_P L} \int_{V_P} n_P(\boldsymbol{r}_1) \left[\frac{d\phi^{(1)}_{1W}}{dr_1} - \sum_{j \in S} \frac{\boldsymbol{r}_j \cdot \boldsymbol{r}_{1j}}{r_j \, r_{1j}} \frac{d\phi_{1j}}{dr_{1j}} \right] d\boldsymbol{r}_1 \tag{13b}$$

where r_j is the radial coordinate of surface atom j.

Although there is some indication from the simulation results currently available for f_s that this quantity is sensitive to the nature of the particle/pore wall interaction, to the authors' knowledge no computations have been reported in which the forces on the individual solid atoms (integrated as a continuum a posteriori or summed

discretely) are considered. Equation (13) addresses this situation in part through the summation over surface atoms, however we still treat the background potential $\phi_W^{(1)}$ as a two-body interaction.

In the computation of the diffusion coefficients we have employed two different methods as proposed in [25]. The first method, which follows directly from the force/flux relations of nonequilibrium statistical mechanics, provides the following equation for the volume averaged axial self-diffusion flux of the tracer

$$J_{1*z} = - D_{1*P}^{(z)} \frac{\partial n_{1*P}}{\partial z} \tag{14}$$

where

$$D_{1*P}^{(z)} = \frac{N}{N-1} \Omega_{1*1*}^{(z)} \tag{15}$$

$$\Omega_{1*1*}^{(z)} = \frac{1}{N} \sum_{i=1}^{N} \int_0^\infty dt \, \langle v_{iz}(o) v_{iz}(t) \rangle \tag{16}$$

$D_{1*P}^{(z)}$ is the diffusion coefficient for the tracer in the pore, n_{1*P} is the pore phase tracer number density, and the term inside the integral in Equation (16) is the velocity autocorrelation function for particle i averaged over an equilibrium ensemble.

Equation (15) is most appropriate for situations in which the fluid particle axial momentum is conserved during a collision with the pore wall and this is the condition employed in the simulations for pores described by Equation (1). If the axial momentum of the particle is not conserved during a collision due to elastic or inelastic backscattering, then a more convenient method of analysis based on the inversion procedure proposed by Mason and Viehland [32] leads to the following expression for $D_{1*P}^{(z)}$

$$\frac{1}{D_{1*P}^{(z)}} = \frac{1}{D_{1*M}^{(z)}} + \frac{1}{D_{1*1}^{(z)}} \tag{17}$$

where

$$D_{1*M}^{(z)} = N \Omega_{oo}^{(z)} \tag{18}$$

$$D_{1*1}^{(z)} = N \Omega_{oo}^{(z)} \left[\frac{\Omega_{1*1*}^{(z)} - \Omega_{oo}^{(z)}}{N \Omega_{oo}^{(z)} - \Omega_{1*1*}^{(z)}} \right] \tag{19}$$

and

$$\Omega_{oo}^{(z)} = \int_0^\infty dt \, \langle \, u_{oz}(o) u_{oz}(t) \, \rangle$$

in which $u_{oz}(t)$ is the instantaneous mass average velocity of the pore fluid at time t.

Combining Equations (18) and (19) we find

$$D_{1*P}^{(z)} = \frac{N}{N-1} \left(\Omega_{1*1*}^{(z)} - \Omega_{oo}^{(z)} \right) \tag{21}$$

which differs from Equation (15) by the term $\Omega_{oo}^{(z)}$. This term, however, scales as $1/N$ and approaches zero in the thermodynamic limit $N \to \infty$. Equations (17)–(21) are the theoretical results which have been used here to analyze the molecular dynamics data for the volume averaged axial diffusion coefficients within pores described by Equation (2).

Finally, as mesaures of the influence of the wall on the mobility of the fluid particles we may consider approximate expressions for the local diffusion coefficients similar in form to the above equations for a volume element ΔV of the system by replacing $\Omega^{(z)}_{1*1*}$ and $\Omega^{(z)}_{oo}$ by the coefficients

$$\frac{N}{\langle N(\Delta V) \rangle} \Omega^{(z)}_{1*1*}(\Delta V); \frac{N}{\langle N(\Delta V) \rangle} \Omega^{(z)}_{oo}(\Delta V)$$

where

$$\Omega^{(z)}_{1*1*}(\Delta V) = \frac{1}{N} \sum_{i=1}^{N} \int_0^\infty dt \, \langle v_{iz}(0,\Delta V) v_{iz}(t) \rangle \tag{22}$$

$$\Omega^{(z)}_{oo}(\Delta V) = \frac{1}{N} \sum_{i=1}^{N} \int_0^\infty dt \, \langle v_{iz}(0,\Delta V) u_{oz}(t) \rangle \tag{23}$$

and $\langle N(\Delta V) \rangle$ is the ensemble averaged number of fluid particles in ΔV. $v_{iz}(0,\Delta V)$ in Equations (22) and (23) is the axial component of the velocity of a particle i which starts its trajectory in ΔV at time $t = 0$. In section 3 these expressions will be used to examine the radial dependence of the mobility of the fluid particles in the two largest structured pores considered in these studies. A similar analysis for the structureless model will be based on the approximate kinetic theory of Davis [23] which, as will be shown below, provides reasonably accurate diffusion coefficients in this case for pores larger than $R^*_{PEFF} = 1$.

3. DISCUSSION OF RESULTS

The results to be presented here will be expressed relative to the corresponding parameters for the bulk homogeneous liquid at the same temperature ($T* = 1.15$) and chemical potential ($\mu/kT = -10.954$ as defined in the appendix). The bulk liquid density under these conditions is $n^*_B = 0.608(7)$ and the reduced pressure P^*_B ($= P_B\sigma^3/kT$) is 0.20(2) which was obtained using the Irving-Kirkwood [33] pressure tensor. These results as well as others to be provided below do not include longe-range corrections beyond the cut-off radius $R^*_c = 3.3$. A bulk fluid molecular dynamics simulation at the same temperature and density also gave

$$D_{1*B} = 0.169(6) \sqrt{\varepsilon\sigma^2/m}$$

The above results for P^*_B and D_{1*B} are in good agreement with those reported by Magda et al [11] for a Lennard-Jones liquid under similar conditions.

3.1 Structureless Pore Walls

Equilibrium properties

The properties and Monte Carlo simulation results for pores described by Equation (1) are presented in Table 1, and in Figure 3(a) we plot the partition coefficients, obtained using Equation (5) with $\langle n_P \rangle = \langle N \rangle / 2\pi R^2_{PEFF} L$, as a function of particle reduced radius λ. The solvation forces reduced by the bulk pressure are plotted in the same manner in Figure 3(b). Both of these graphs are similar in form to those given in [26, 31] for a hard-sphere fluid at a bulk density $n^*_B = 0.6$ distributing into cylindrical pores. The local maxima in K and f_s occur when integer layers of fluid

particles are preferentially formed within the pore and for intermediate pore sizes, as indicated by the upper abscissae in Figures 3(a) and 3(b), ill-fitting layers result in a lowering of both these parameters. It is also of interest to note that the magnitude of the partition coefficient at any given value of λ is quite close to the corresponding result for the hard-sphere fluid and this will serve an important purpose in the discussion of the MD simulation results for diffusion to be presented later. However, at this point, we observe that the near equality of the pore fluid densities in both cases is fortuitous and the low values of K shown in Figures 3(a) are primarily a result of the relatively weak attractive interaction predicted by Equation (1). We can expect significantly different values for K if the particle/wall potential parameter ε_{iW} is either decreased (towards nonwetting) or increased (improved wettability and adsorption).

The solvation forces are also characteristic of strong repulsive interactions between the particles of the pore fluid and the pore wall and the reasons for this are most clearly illustrated by examining the density profiles. In Figure 4 we plot these profiles for two representative pore sizes and we observe that although the profiles are distinctly different in overall shape the solvation forces in both cases are nearly equal. On closer inspection it can be seen that the densities in the vicinity of the peak nearest the pore wall are similar and it is this region of the profile which largely determines the magnitude of f_s. This fact coupled with the weak attractive and steeply rising repulsive particle/pore wall interaction shown in Figure 2 is the principal cause for the large positive solvation forces determined in the simulations.

In Figures 3(b) and 4 we also provide theoretical results predicted by two approximations to the YBG equation. By expressing the particle/particle potential energy function in a form similar to the Weeks-Chandler-Anderson perturbation scheme with the reference state represented as a hard-sphere interaction, it may be shown [4,23] that the YBG singlet density equation can be written as

$$kT\nabla \ln n_{\mathrm{P}}^{*}(\boldsymbol{r}*) = -\nabla\phi_{\mathrm{w}}(\boldsymbol{r}^{*}) + \int n_{\mathrm{P}}^{*}(\boldsymbol{r}* + \boldsymbol{s})\, g_1(\boldsymbol{r}*, \boldsymbol{r}* + \boldsymbol{s})\, \frac{\boldsymbol{s}}{s}\frac{\mathrm{d}\phi^{\mathrm{P}}}{\mathrm{d}s}\,\mathrm{d}\boldsymbol{s} - kT\int n_{\mathrm{P}}^{*}(\boldsymbol{r}* + \boldsymbol{k})\, g_2(\boldsymbol{r}*, \boldsymbol{r}* + \boldsymbol{k})\, \boldsymbol{k}\, d\boldsymbol{k} \tag{24}$$

Table 1 System Characteristics and GCEMC Simulation Results for Pores with Structureless Walls (Wall I)

[a]R_{P}^{*}	[a]R_{PEFF}^{*}	[a]λ	[a]L^{*}	$\langle N\rangle$	[b]$\langle f_s^{*}\rangle$
3.000	2.737	0.183	7.111	159.8(1.1)	0.385(11)
2.167	1.900	0.263	13.635	132.8(0.7)	0.482(14)
1.929	1.659	0.301	17.211	123.4(0.6)	0.699(18)
1.750	1.478	0.338	20.898	108.4(0.3)	0.566(15)
1.500	1.223	0.409	28.444	101.5(0.4)	0.895(20)
1.333	1.049	0.477	36.000	73.4(0.6)	0.898(16)
1.214	0.921	0.543	43.395	64.3(0.6)	0.561(06)
1.125	0.820	0.610	50.568	71.2(0.4)	0.683(02)
1.056	0.734	0.681	57.465	79.4(0.3)	0.912(04)
0.917	0.602	0.830	76.193	87.0(0.3)	1.775(07)
0.885	0.583	0.858	81.820	73.5(0.6)	1.768(11)
0.833	0.559	0.894	92.156	16.3(0.3)	0.521(08)

[a] R_{P}, R_{PEFF}^{*} and L^{*} are reduced by σ and $\lambda = 1/2R_{\mathrm{PEFF}}^{*}$.
[b] $\langle f_s^{*}\rangle$ is the solvation force reduced by kT/σ^{3}.
The number of GCEMC compound events generated in each run was 5×10^{6} of which the first 1×10^{6} were rejected.

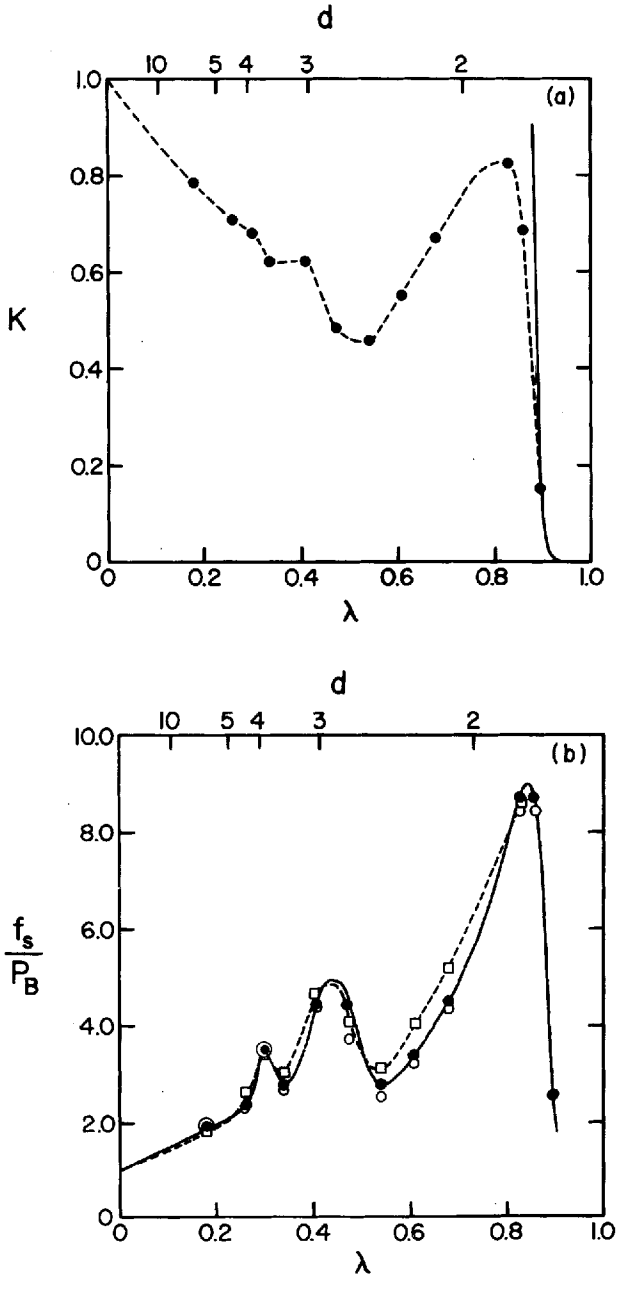

Figure 3 Volume averaged equilibrium properties as a function of particle reduced radius λ for the Lennard-Jones liquid in pores with structureless walls. The upper abscissa, d, is the diametric distance between pore wall surface atoms. (a) The partition coefficient. – –●– – GCEMC simulation results;——— Henry's law. (b) The solvation force reduced by the bulk hydrostatic pressure. —●— Simulation results; □ Fischer-Methfessel approximation; ○ bulk fluid approximation.

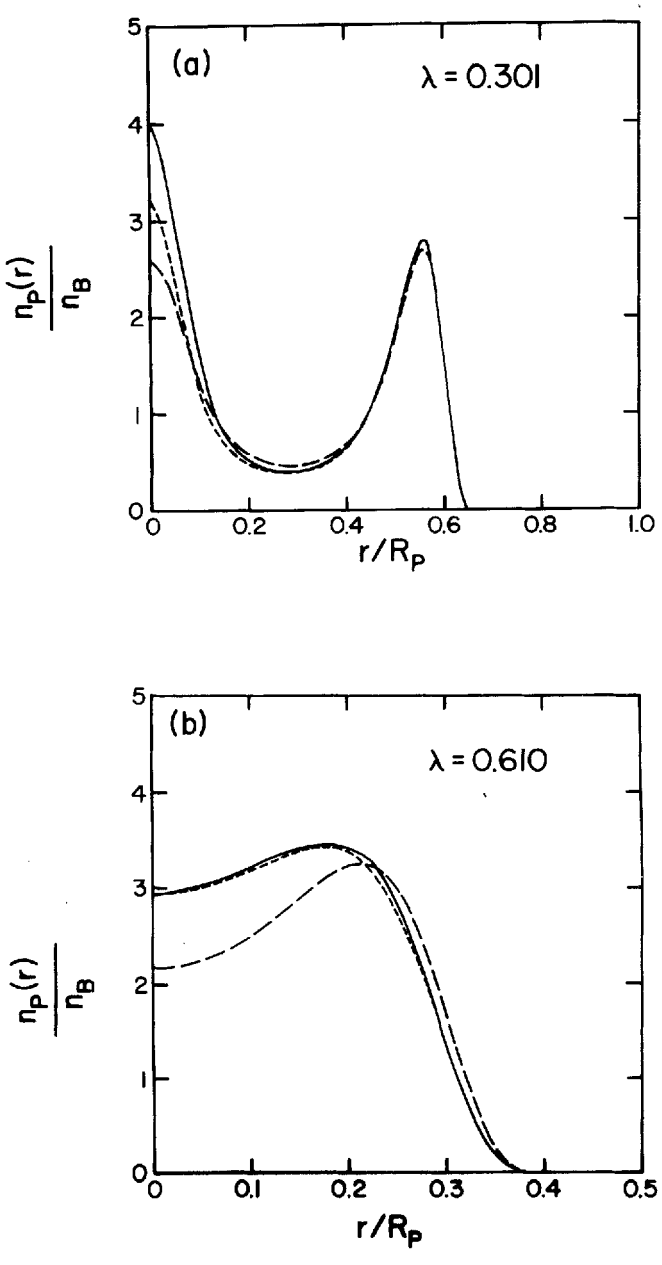

Figure 4 Radial density profiles in pore model 1 (structureless pore walls). ——— Simulation; – – – YBG equation (Fischer-Methfessel approximation); – – – – YBG equation (bulk fluid approximation).

where

$$\phi^{P}(s) = -\varepsilon \quad s < 2^{1/6}$$
$$= \phi_{LJ}(s) \quad s > 2^{1/6}$$

and $\phi_{LJ}(s)$ is given by Equation (4). The last term in Equation (24) is the hard-core contribution and the $d\boldsymbol{k}$ integration is over the solid angle. For simplicity, we also assume that the reference hard-sphere diameter is equal to σ.

The two approximations which we have considered here refer to assumed forms for the pair correlation functions g_1 and g_2 in Equation (24). In their original work Fischer and Methfessel [4] proposed the following

$$g_1(\boldsymbol{r}*, \boldsymbol{r}* + \boldsymbol{s}) = 1.0 \tag{25}$$

and

$$g_2(\boldsymbol{r}*, \boldsymbol{r}* + \boldsymbol{k}) = g_B^{HS}\left(1, \vec{n}_P^*(\boldsymbol{r}* + \frac{1}{2}\boldsymbol{k})\right) \tag{26}$$

Equation (25) is a mean-field approximation and Equation (26) assumes that the inhomogeneous contact pair correlation function in the last term in Equation (24) may be replaced by a uniform hard-sphere contact pair correlation function evaluated at a density $\vec{n}_P^* \cdot \vec{n}_P^*$ is obtained by locally averaging the pore fluid density over a sphere of volume $\pi/6$ (in units of σ^3) centered at $\boldsymbol{r}* + \frac{1}{2}\boldsymbol{k}$.

The second approximation considered here also employs the mean-field assumption for g_1 and replaces g_2 in Equation (24) by

$$g_2(\boldsymbol{r}*, \boldsymbol{r}* + \boldsymbol{k}) = g_B^{HS}(1, n_B^*) \tag{27}$$

Equation (27) is similar to Equation (26) but only requires evaluation of the hard-sphere pair correlation function at the bulk homogeneous density n_B^*. This simplification has been previously used in two studies [1,10] where it was referred to as a superposition approximation. However to avoid confusion with Kirkwood's original theory [34] we will here refer to Equation (27) with Equation (25) as a bulk fluid approximation.

For structureless pore walls the integration scheme required to solve Equation (24) for the density profile is relatively straightforward. With the exact density profiles available as input data for the iterative solution we have employed the trapezoidal rule in a manner similar to that outlined by Vanderlick and Davis [24]. The mesh increment employed on the radial integration was 0.01 R_P^* and, with suitable parameterization of the integrals in the second and third terms on the right hand side of Equation (24) and in the determination of $\vec{n}_P^*(\boldsymbol{r}* + \frac{1}{2}\boldsymbol{k})$, mesh sizes equal to 0.05 were found to provide sufficiently accurate results.

To ensure reasonable consistency between the analysis of the YBG equation and the conditions employed in the simulations the cut-off radius $R_c^* = 3.3$ was incorporated into the second term in Equation (24). The Carnahan-Starling equation for g^{HS} [35] was used to compute the uniform hard-sphere pair correlation functions in Equations (26) and (27) and the integration constant resulting from the radial integration of Equation (24) was determined by normalizing the predicted profile with respect to the actual number of Lennard-Jones particles per unit length of the pore obtained in the simulations.

In comparing the density profiles predicted by the two approximations to the YBG equation with those determined from the computer simulations we generally found that the simpler bulk fluid approximation (Equation (27)) provided the most accurate results. This is clearly seen in Figure 4 and also in the values predicted for f_s using Equation (12b) as shown in Figure 3(b). One of the major reasons for the poorer results in the case of the Fischer-Methfessel approximation lies in overestimation of the importance of the last term in Equation (24) in the vicinity of the pore wall. In this region the integral over the solid angle in both approximations is a negative quantity and its magnitude is sensitive to the functional form assumed for g_2. In the method proposed by Fischer and Methfessel g_2 is quite large in that portion of the solid angle enclosed by the density peak nearest the wall and, since each term in Equation (24) represents a force, the repulsive g_2 contribution now takes on the role of an attractive force drawing the fluid closer to the surface of the solid. This is observed as a partial flattening of the profile in Figure 4(a) and a distinct shift of the fluid towards the positive region of ϕ_W in Figure 4(b). As mentioned earlier the solvation force is primarily determined by the structure of the density peak at the pore wall and the higher than average densities usually predicted by Equation (24) with Equation (26) in this region of the pore result in an overestimation of f_s.

Although the bulk fluid approximation does appear to be the better of the two in the present case this need not be true in general. Fischer and Methfessel have pointed out the difficulty of defining the bulk state in Equation (27) when a liquid/vapor interface is under consideration. For such systems and also for vapor adsorption in pores, Equation (26) has been found to be quite versatile [4,13]. Later in our analysis of the structured pore model we will show that Equation (26) in fact provides a better representation of the density profiles in support of its wider scope of application.

Diffusion

The molecular dynamics simulation results for the pore model with wall 1 are presented in Table 2. The half-lengths L^* employed in these simulations provide the

Table 2 System Characteristics and MD Simulation Results for Pores with Structureless Walls (Wall 1)

[a]ζ	[a]L^*	[b]$N_t(10^{-3})$	[b]$N_t^R(10^{-3})$	T^*	[a]$\langle f_s^* \rangle$	[c]t^*_{max}	[d]$\Omega^{zz}_{\vert*\vert*}$
0.183	8.900	78	6	1.15	0.386(14)	5	0.223(07)
0.263	20.530	88	8	1.13	0.460(17)	5	0.228(07)
0.301	27.886	96	8	1.16	0.699(12)	6	0.246(07)
0.338	38.549	120	10	1.17	0.588(27)	6	0.260(09)
0.409	56.048	140	10	1.15	0.900(22)	6	0.244(11)
0.477	98.075	170	10	1.14	0.894(05)	6	0.300(12)
0.543	134.99	86.4	7.2	1.14	0.558(06)	8	0.249(15)
0.610	142.05	88	8	1.15	0.678(05)	8	0.250(16)
0.681	144.73	93.6	7.2	1.15	0.911(06)	8	0.270(20)
0.830	175.12	192	8	1.13	1.768(19)	8	0.400(19)
0.858	222.62	256	8	1.14	1.756(14)	10	0.549(16)
0.894	1130.17	425	25	1.15	0.520(04)	190	4.3(1.2)

[a] As in Table 1.
[b] N_t is the total number of time steps in the MD trajectory and N_t^R is the number of initial time steps discarded where each time step was $\Delta t^* = 0.005\ \sigma\sqrt{m/\varepsilon}$.
[c] t^*_{max}, in units of $\sigma\sqrt{m/\varepsilon}$, is the maximum integration time employed in equation (16).
[d] $\Omega^{zz}_{|*|*}$ is the axial phenomenological coefficient calculated using Equation (16) and reduced by $\sigma\sqrt{\varepsilon/m}$.
The total number of particles employed in each run was 200.

pore volume needed to accommodate 200 particles at the same density as in the GCEMC computations and for comparative purposes we provide the solvation forces determined from the MD trajectories. These results agree with those given in Table 1 within computational error. The density profiles obtained from the MD simulations were also found to be in excellent agreement with the GCEMC results shown in Figure 4.

The phenomenological coefficients $\Omega^{(z)}_{1*1*}$ determined using Equation (16) are given in the last column of Table 2, and the tracer diffusion coefficients calculated using these results and reduced by D_{1*B} are plotted as a function of particle reduced radius in Figure 5. In comparing these diffusion coefficients with prior simulations reported in the literature we make the following observations:

(a) In all cases the pore diffusion coefficients shown in Figure 5 are larger than D_{1*B}. This is in marked contrast to the earlier results obtained for hard-sphere fluids in cylindrical pores with specularly reflecting hard walls [25]. It is also of interest at this point to recall our earlier observation that the bulk and pore fluid

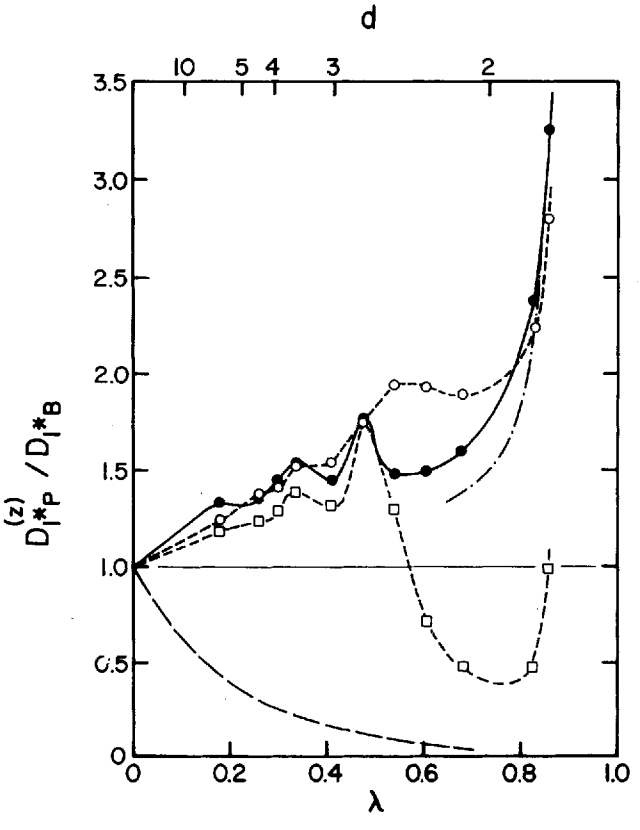

Figure 5 Reduced axial diffusion coefficient for the tracer as a function of λ in pores with wall 1. d as in Figure 3. —●— MD simulation; – – □ – – Davis-Enskog kinetic theory (Fischer-Methfessel approximation); – – ○ – – Davis-Enskog kinetic theory (bulk fluid approximation); – · – · – hard-rod model (Equation (31)); – – – the empirical correlation of Satterfield et al [21].

densities employed in the hard-sphere studies were similar to those employed here.

(b) The oscillatory behaviour of $D^{(z)}_{1*P}$ as a function of λ and the corresponding trends in K as shown in Figure 3(a) correlate very well. In fact $D^{(z)}_{1*P}/D_{1*B}$ appears to be approximately equal to $1/K$ over most of the range of pore sizes investigated. This observation is in agreement with results obtained by Magda et al [11] for self diffusion in Lennard-Jones fluids confined within slit-shaped pores. The hard-sphere pore diffusion coefficients reported in [25] do not, however, exhibit any correlation with the averaged pore phase density except in the range $\lambda < 0.8$ and also for pores larger than $1/\lambda \sim 5$.

Although the pore diffusion coefficients for the Lennard-Jones system appear to be directly related to n_p it is clear from the above observations that the transport characteristics of fluids in pores cannot generally be related to pore averaged static properties in a simple way. A deeper understanding of the phenomena involved must rely on an analysis of the local pore fluid structure and dynamics. Here we offer a qualitative explanation for the difference between the hard-sphere and Lennard-Jones results by considering the modified Enskog theory for inhomogeneous fluids recently proposed by Davis [23]. This approximate theory provides an expression for the tracer friction coefficient in terms of local structural correlations and assumes that dynamical correlations are negligible.

The general expression for the local axial friction coefficient divided by its bulk value is given by Davis' theory as

$$\frac{\zeta^{(z)}_{1*P}(\boldsymbol{r}^*)}{\zeta_{1*B}} = \frac{3}{2\pi}\int_0^{2\pi}\int_{-1}^{1} g^*(\boldsymbol{r}^*, \boldsymbol{r}^* + \boldsymbol{k})\frac{n_P(\boldsymbol{r}^* + \boldsymbol{k})}{n_B}(1 - u^2)\sin^2\psi \, du \, d\psi \quad (28)$$

where

$$g^*(\boldsymbol{r}^*, \boldsymbol{r}^* + \boldsymbol{k}) = \frac{g_2(\boldsymbol{r}^*, \boldsymbol{r}^* + \boldsymbol{k})}{g_B^{HS}(1, n^*_B)} \quad (29)$$

The inverse of Equation (28) is equal to the local diffusion coefficient within the pore reduced by D_{1*B} and is only a function of the radial coordinate r for the structureless model. The volume averaged axial diffusion coefficient, which is the quantity determined in the simulations, may also be shown to be given by

$$\frac{D^{(z)}_{1*P}}{D_{1*B}} = \frac{1}{N}\int_{V_P}\frac{\zeta_{1*B}}{\zeta^{(z)}_{1*P}(r)} n_P(\boldsymbol{r}) \, d\boldsymbol{r} \quad (30)$$

Equations (28) and (30) were incorporated into the computer program employed in the analysis of the YBG equation and the results obtained using the bulk fluid and Fischer-Methfessel approximations for g_2 are shown in Figure 5. For pores larger than twice the size of the Lennard-Jones particles the diffusion coefficients predicted by Davis' theory are in good agreement with the simulations. Quantitatively the bulk fluid approximation is better for reasons similar to those given earlier in the discussion of the density profiles, however the Fischer-Methfessel approximation does appear to provide better qualitative predictions of the oscillatory behaviour of $D^{(z)}_{1*P}$.

For smaller pores ($\lambda < 0.5$) the results are very poor and we believe the primary reason for this rests with Equation (28) rather than the approximate expressions assumed for g_2. It is particularly interesting to note the poor quality of the bulk fluid

approximation even though Equation (27) provides excellent density profiles in this range of pore sizes (see for example Figure 4(b); the theoretical analysis given in [10] for narrow slit pores is also of interest in this respect). In the range $0.5 < \lambda < 1.0$ the pore fluid under goes a transition from three-dimensional to one-dimensional behaviour with a consequent contraction in the phase-space available to the fluid particles. Under these conditions it is unlikely that a three-dimensional kinetic equation of the type employed in the derivation of Equation (28) will adequately describe the transport process. This is illustrated in Figure 5 where we also show results predicted by the one-dimensional hard-rod model which provides the following expression for the diffusion coefficient [25,36]

$$\frac{D_{1*P}^{HR}}{D_{1*B}} = \frac{32\lambda^2}{3\pi\sqrt{2}} \frac{g_B(1,n_B^*)}{KC(n_B^*)} \left[1 - \frac{\pi K n_B^*}{4\lambda^2}\right] \tag{31}$$

where $C(n_B^*)$ is a density dependent correction factor required to bring the bulk phase Enskog diffusion coefficient, D_{1*B}, into agreement with simulation results [37,38]. Above $\lambda \sim 0.825$ Equation (31) is in very good agreement with the simulation results and is better than Equation (28) in predicting $D_{1*P}^{(z)}$ over the range $0.65 < \lambda < 0.825$.

Although it is not possible to use Equation (28) to predict $D_{1*P}^{(z)}$ over the entire range

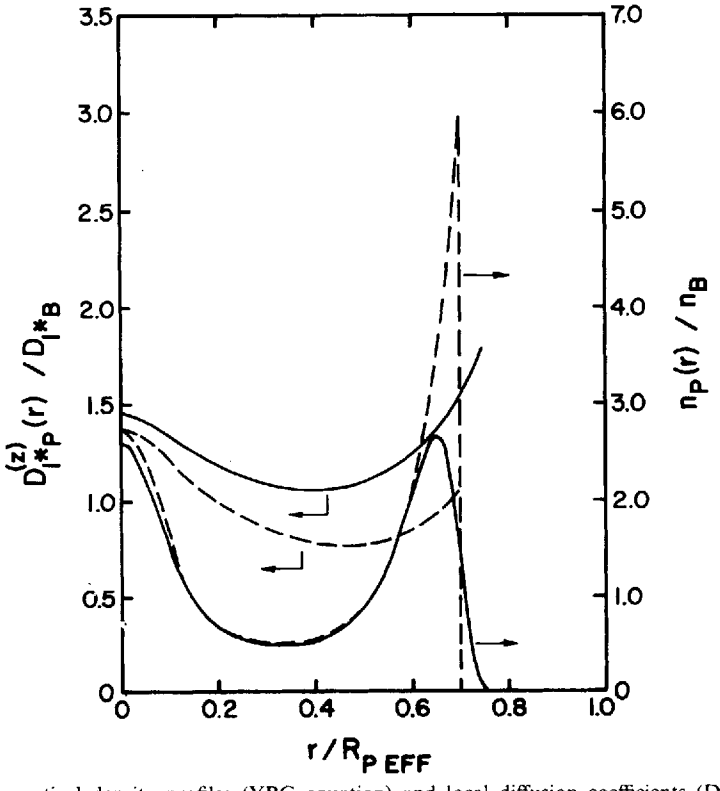

Figure 6 Theoretical density profiles (YBG equation) and local diffusion coefficients (Davis-Enskog kinetic theory) with g_2 given by the Fischer-Methfessel approximation. —— Lennard-Jones liquid/structureless pore wall ($\lambda = 0.301$, $n_B^* = 0.608$, $\langle n_P^* \rangle = 0.42$); – – – hard-sphere fluid/hard cylindrical pore wall ($\lambda = 0.3$, $n_B^* = 0.6$, $\langle n_P^* \rangle = 0.47$). R_{PEFF} is the characteristic pore radius (Equation 10)).

of particle reduced radii $0 \leqslant \lambda \leqslant 1$, the accuracy of Davis' theory in pores larger than $1/\lambda = 2.0$ does permit an investigation into the reasons for the different trends observed here for the Lennard-Jones fluid and in [25] for a hard-sphere fluid confined in pores with specularly reflecting walls. In Figure 6 we plot theoretical results for the density profiles and for the local diffusion coefficients predicted by Equations (24) and (28) respectively using the Fischer-Methfessel approximation for g_2. Both the Lennard-jones results ($\lambda = 0.301$, $n_B^* = 0.608$) and the hard-sphere results ($\lambda = 0.3$, $n_B^* = 0.6$) for the density profiles are observed to be in very close agreement except at the pore wall where the hard-sphere peak density is more than twice as large as the Lennard-Jones value. This behaviour is also observed in the exact density profiles shown here in Figure 4(a) and in Figure 1 of reference [25] and we may conclude that the density peak at the pore wall is the cause for the disparity between the diffusion coefficients in both systems. This is clearly seen in the theoretical results obtained for the local diffusion coefficients and is further amplified in the volume averaged values for $D_{1*P}^{(z)}$ due to the density weighting in Equation (30). For the conditions considered in figure 6 the theoretical results for $D_{1*P}^{(z)}/D_{1*B}$ are 0.91 (hard sphere/hard wall) and 1.29 (Lennard-Jones/structureless wall) and both of these values are approximately 12% lower than the corresponding MD diffusion coefficients. Additional computations not reported here for the hard-sphere system also provided results similar to Figure 6 with volume averaged diffusion coefficients in favorable agreement with those reported in [25].

To conclude this section we now briefly consider the implications of the lower curve shown in Figure 5. This curve corresponds to an empirical correlation proposed by Satterfield et al [21] for the "tortuosity" corrected diffusion coefficient of molecular solutes in liquid-filled micropores and, in contrast to the MD simulation results for the structureless model, the experimental results represented by this correlation display a completely different trend in the pore size dependence of the diffusion coefficient. The principal reason for this, as mentioned in the introduction, is the omission of a mechanism for axial backscattering of the fluid particles off the pore wall. We may infer from the results presented in [39] that pore space geometry and topology in porous media similar to the silica-alumina catalyst beads employed by Satterfield et al [21] can play an important role in hindered diffusion, however additional effects arising from the microscopic details of the solid surface, as indicated by the need for diffuse scattering modifications [25,26,39], should be taken into consideration. An increase in the particle/wall potential parameter ε_{iW} in Equation (1) will certainly lead to more highly structured density profiles and, by inference from the above discussion on the importance of the density peak at the pore wall, this should result in lower diffusion coefficients. However, one physical property which will not be influenced by adjusting a continuum potential in this way is perfect slip of the pore fluid parallel to the solid surface. Slip conditions of this type will generally lead to low friction coefficients at the solid/fluid interface, as indicated by the results shown in Figure 6, and only by imposing a diffuse mode of reflection or, preferably, by introducing atomic structure into the solid surface will the momentum transfer characteristics of the pore fluid be simulated in a realistic manner.

3.2 Structured Pore Walls

Equilibrium properties

The system characteristics and volume averaged equilibrium properties for the Lennard-Jones liquid in pores described by Equation (2) are presented in Table 3, and

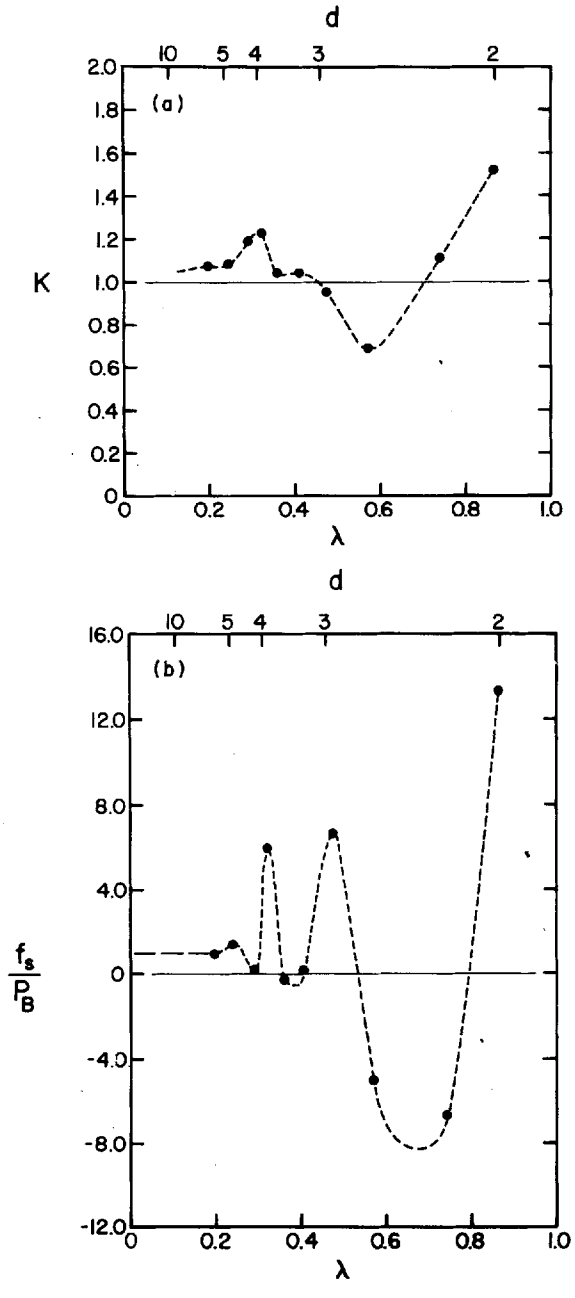

Figure 7 Volume averaged equilibrium properties as a function of particle reduced radius λ for the Lennard-Jones liquid in pores with structured walls. d as in Figure 3. (a) GCEMC simulation results for the partition coefficient; (b) simulation results for the solvation force reduced by the bulk hydrostatic pressure.

Table 3 System Characteristics and GCEMC Simulation Results for Pores with Structured Walls (Wall 2)

[a]N_R	[b]R_P^*	[b]R_{PEFF}^*	[b]λ	[b]L^*	$\langle N \rangle$	[b]$\langle f_{s^*} \rangle$
18	2.879	2.500	0.200	7.5	192.0(1.8)	0.181(67)
15	2.405	2.020	0.247	11.0	185.6(1.1)	0.272(53)
13	2.089	1.698	0.294	14.5	190.6(2.0)	0.034(80)
12	1.932	1.538	0.325	17.0	189.1(1.0)	1.198(43)
11	1.775	1.374	0.364	20.5	154.1(0.7)	−0.057(25)
10	1.618	1.211	0.413	24.5	143.3(0.7)	0.023(34)
9	1.462	1.045	0.478	30.0	119.4(0.5)	1.345(32)
8	1.307	0.871	0.574	37.5	74.3(0.1)	−1.016(07)
7	1.152	0.671	0.745	48.0	92.1(0.4)	−1.346(11)
6	1.000	0.577	0.867	64.0	123.2(0.2)	2.698(04)

[a] N_R is defined in Equation (3).
[b] As in Table 1.
The number of GCEMC compound events generated in each run was 5×10^6 except for $N_R = 18$ where the number of events was 7×10^6. The initial 1×10^6 events (or 1.5×10^6 for $N_R = 18$) were discarded.

in Figure 7 both K and f_s/P_B are plotted as functions of the particle reduced radius λ. These results are comparable with the results obtained for the structureless model in only one respect, local maxima in K and f_s occur approximately at integer values of d and local minima are observed at intermediate pore sizes. For pores larger than twice the size of the fluid particles the partition coefficient is close to 1.0 or slightly greater and this is consistent with an empirical observation in pore volume analysis known as Gurvitsch's rule [40]. In the smaller pores however, lateral filling is restricted to a single fluid particle and in the transition region at $\lambda = 0.5$ the partition coefficient drops sharply. Above $\lambda = 0.5$ the results for $\langle N \rangle$ given in Table 3 show that the average pore occupancy corresponds to one fluid particle per cage (as defined in Figure 1(b)) and the reduction in pore volume in going from $N_R = 8$ to $N_R = 6$ leads to an increase in K over this range of pore sizes.

Contrasts between the structured and structureless models are also very apparent in the results obtained for the solvation force. Not only are the amplitudes of the oscillations much larger for wall 2 but we also observe zero or negative tensile forces in pores with noninteger fluid layers. Large positive compressive forces and negative tensile forces of this type have been observed in experiments on fluids confined between flat mica sheets [14–16] and although the pore space involved in these experiments is slit-like, this does not preclude the existence of similar effects in cylindrical systems. These forces may indeed play a contributing role in the stability of membrane pore configurations, helical macromolecules, and in hexagonal-lamellar liquid crystalline phase transitions in microemulsions.

Modulation in the behaviour of both K and f_s in pores described by Equation (2) is accompanied by highly structured density profiles. This is illustrated in Figure 8 where the z and θ averaged density profiles for two pores with structured walls are compared with results obtained for the structureless model at similar values of λ. In this figure we observe that the oscillations in $n_P(r)/n_B$ are typically a factor of two larger in the structured systems due primarily to the much deeper particle/pore wall potential minima involved in this case as shown in Figure 2. The intrinsic lattice structure of the solid surface however, also plays an important role and this is clearly demonstrated in Figures 9 and 10. These figures correspond to θ averaged profiles for particles at axial position 1 in Figure 1(b) (the pore window) and at axial position 2

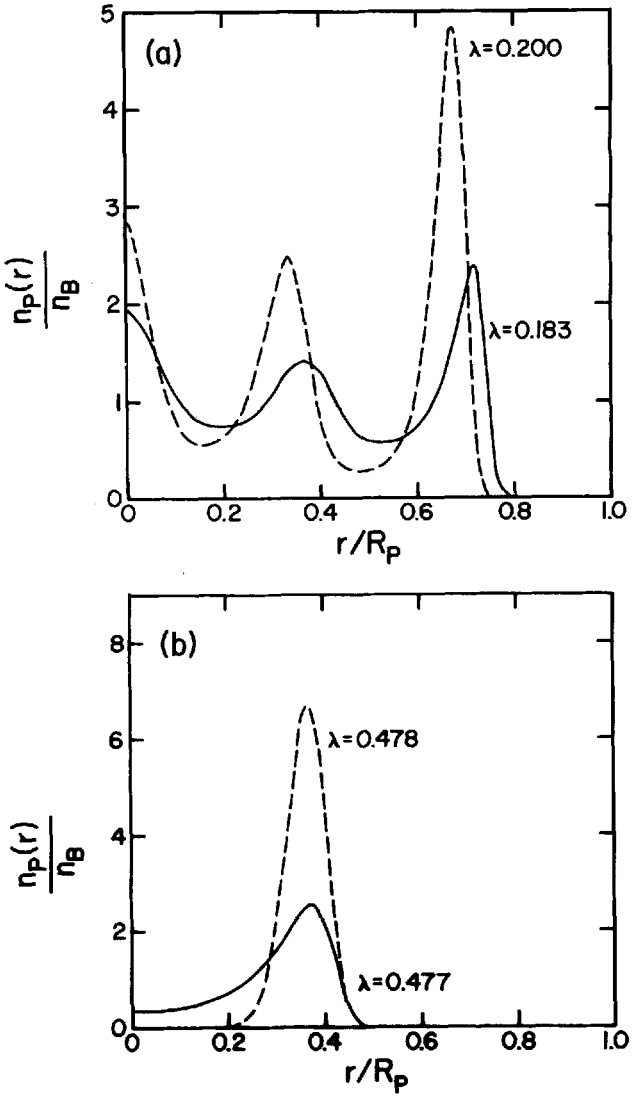

Figure 8 Radial density profiles in the two model pores. —— Structureless pore walls; – – – z and θ averaged profiles in pores with structured walls.

in the same figure (the polygonal cage) respectively. The profiles for $N_R = 6$ and 7 have been omitted for clarity. However as a guide to the general trends in the peak magnitudes we note that in the pore window the peak maximum for $N_R = 6$ was found to be $n_P(r)/n_B = 0.086$, and for $N_R = 7$ $n_P(r)/n_B = 2.68$ with the position of the single peak in both cases occurring at $r/R_P = 0$. In the polygonal cage the peak maxima were $n_P(r)/n_B = 311.0$ for $N_R = 6$ at $r/R_P = 0$ and $n_P(r)/n_B = 28.8$ for $N_R = 7$ at $r/R_P = 0.125$ (in this case $n_P(r)/n_B = 24.7$ at $r = 0$).

Figures 9 and 10 illustrate very strong localization of the fluid particles within the polygonal cage of each pore even though the difference between the particle/pore wall potential energy minima in the cage and the window is only $\sim kT$ which, in itself, is less that 15% of the average well depth shown in Figure 2. Only in the smallest pore where $N_R = 6$ is the energy barrier much larger as indicated by the results cited above

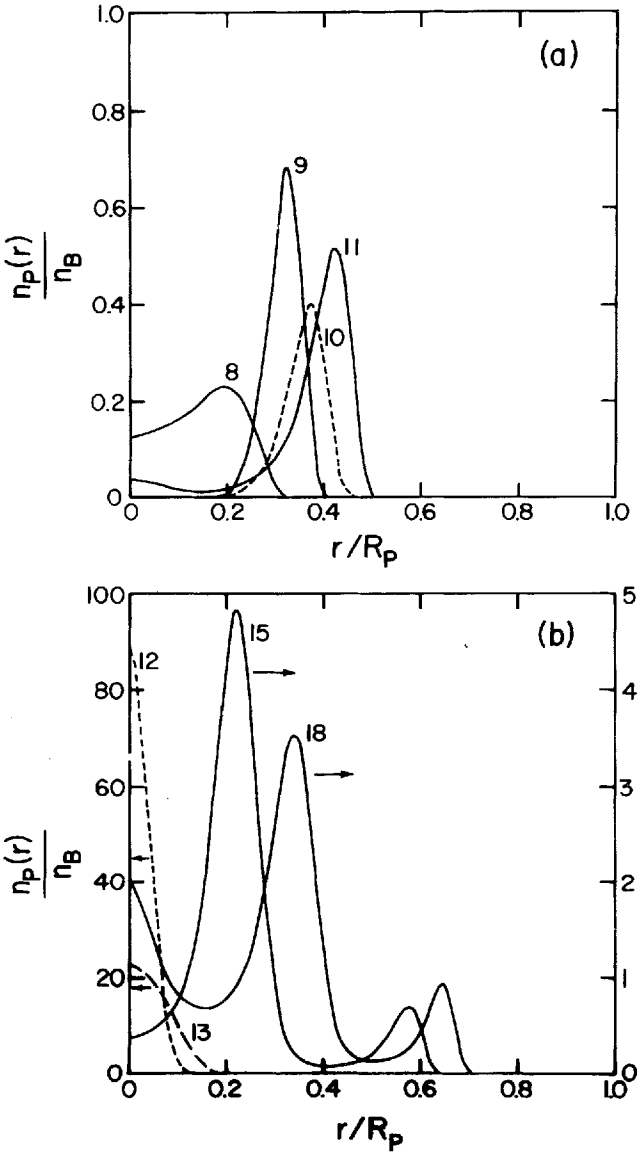

Figure 9 θ averaged radial density profiles for the fluid in the window (axial position 1, Figure 1(b)) of pore model 2. The numbers next to each profile refer to the value of N_R in Equation (3).

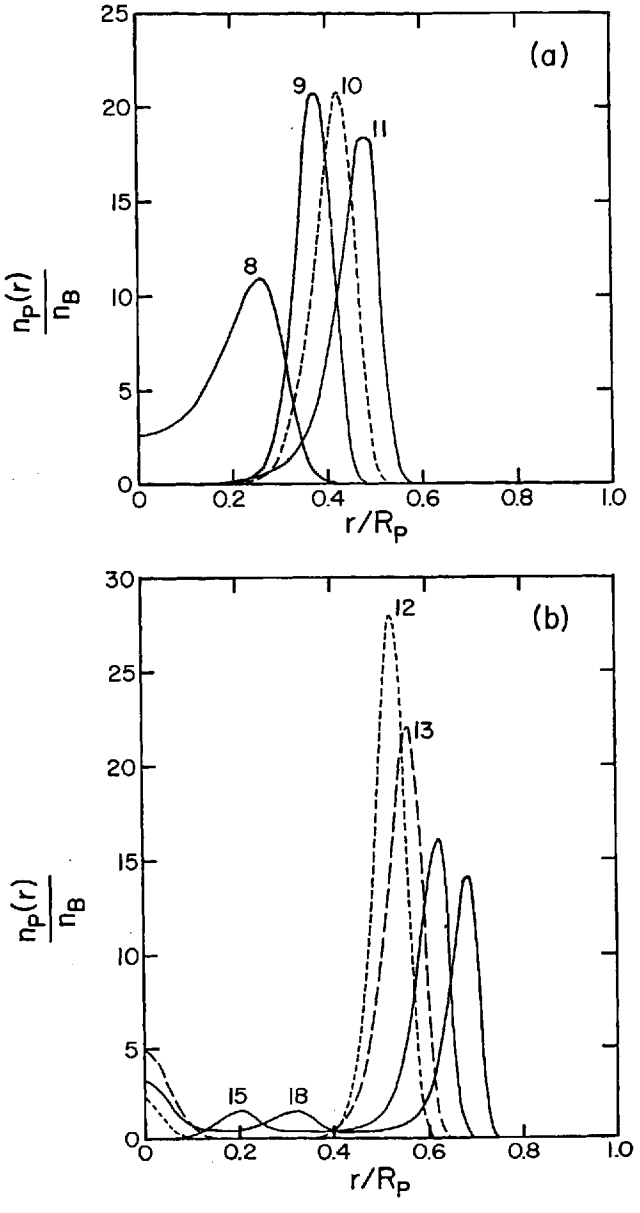

Figure 10 As in Figure 9 but at axial position 2 (Figure 1(b)) within the polygonal cage.

for the peak densities. In this case localization is essentially complete due to the close-packed hexagonal structure of the ring of solid atoms forming the pore window.

An analysis of the YBG equation using the Fischer-Methfessel and bulk fluid approximations has also been considered for the structured model. In this case,

however, the numerical integration scheme is computationally demanding due to the r,z and θ dependence of the local pore fluid density and for this reason we have only examined one pore size to test the capability of both Equations (26) and (27) to reproduce the exact density profiles. The pore considered was $N_R = 8$ due to the very weak θ dependence of the particle/pore wall potential (Figure 2(d)) and this ensures comparative ease in the numerical integration without too fine a grid spacing in the tangential direction. This pore size ($\lambda > 0.5$) was also chosen as an extreme test case in view of the apparent accuracy observed in the profiles predicted by the bulk fluid approximation in very small pores with structureless walls (Figure 4(b)).

By assuming that the mean-field approximation for g_1 is applicable then line integration of Equation (24) provides

$$kT \ln n_p^*(\boldsymbol{r}^*) = -\phi_W^{(2)}(|\boldsymbol{r}^* - \boldsymbol{r}_W^*|) - \int n_p^*(\boldsymbol{r}_1^*)\phi^P(|\boldsymbol{r} - \boldsymbol{r}_1^*|)\, d\boldsymbol{r}_1^* - kT \int_0^1 \int g_2(\alpha \boldsymbol{r}^*, \alpha \boldsymbol{r}^* + \boldsymbol{k})\, n_p^*(\alpha \boldsymbol{r}^* + \boldsymbol{k})\, \boldsymbol{k} \cdot \boldsymbol{r}^* d\boldsymbol{k} d\alpha + C \quad (32)$$

where C is a constant of integration which is determined by normalizing $n_p^*(\boldsymbol{r}^*)$ in a manner similar to that described earlier for the structureless model.

Integration of Equation (32) with Equations (26) and (27) was carrried out for $N_R = 8$ using the trapezoidal rule in a wedge with limits $0 \leqslant r^* \leqslant R_p^*, 0 \leqslant z^* \leqslant 0.5$, and $0 \leqslant \theta \leqslant \pi/N_R$. The mesh increments employed were $0.01R_p^*$, 0.02, and $0.2\pi/N_R$ respectively and the integrals over the solid angles were evaluated on a 25×25 grid. In the spherical radial integration in the second term on the right hand side of Equation (32) and also in the evaluation of the Fischer-Methfessel coarse-grained density $\bar{n}_p^*$ a mesh size of 0.05 was employed.

The results obtained for the θ averaged profiles with partial z averaging over increments of $\Delta z^* = 0.1$ at axial positions 1 and 2 (Figure 1 (b)) are shown in Figure 11. In this case the bulk fluid approximation appears to be the poorer of the two methods particularly in the pore window where the density peak is predicted to be an order of magnitude larger than the exact value. This is in part due to underestimation of the hard-core contribution in Equation (32). The Fischer-Methfessel approximation is quantitatively better in the pore window and correctly predicts the magnitude of the peak inside the cage. However, in the latter case we again observe a significant shift of the density profile towards the positive region of ϕ_W. This is also reflected in the theoretical estimates for the solvation force $f_s/P_B = -3.02$ (Fischer-Methfessel approximation) and $f_s/P_B = -6.37$ (bulk fluid approximation) as compared with the simulation result -5.08.

Although the qualitative appearance of the profiles obtained using Equation (26) is fair, one serious problem which was encountered during the computations arose in the estimated values of the locally coarse-grained density $\bar{n}_p^*$ and hence g_2. Over approximately 12% of the three-dimensional grid $\bar{n}_p^*$ was found to be greater than $\sqrt{2}$, the closest packing density for the hard-sphere system. The profiles shown in Figure 11 were obtained by arbitrarily applying $\sqrt{2}$ as the upper bound on the allowed values of $\bar{n}_p^*$ however this is clearly not a very satisfactory procedure. Recently, Fischer and Heinbuch [41] have examined the relationship between the approximation entailed in Equation (26) and free energy density functional theories and it was shown that this equation represents one member of a class of approximations in which the averaged density is defined by

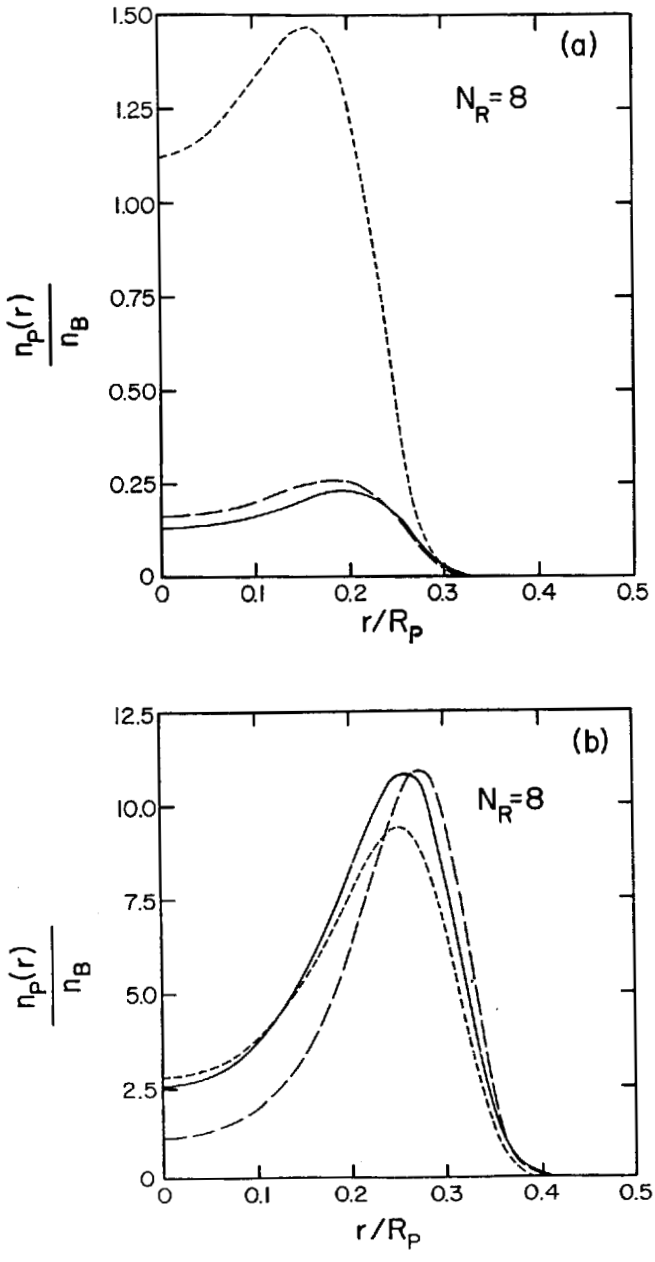

Figure 11 Comparison of the θ averaged radial density profiles with theory in pore model 2. The pore size corresponds to $N_R = 8$ in Equation (3). (a) Axial position 1 (Figure 1(b)). —— Simulation; – – – YBG equation (Fischer-Methfessel approximation); - - - - YBG equation (bulk fluid approximation). (b) As in (a) but at axial position 2 (Figure 1 (b)) within the polygonal cage.

$$\bar{n}_p^*(\boldsymbol{r}_1^*) = \int n_p^*(\boldsymbol{r}_2^*)\,\tau(\boldsymbol{r}_1^* - \boldsymbol{r}_2^*)\,d\boldsymbol{r}_2^* \tag{33}$$

where $\tau(\boldsymbol{r})$ is a weighting function. The coarse-grained density in Equation (26) employs a weighting function $\tau(\boldsymbol{r}_1^* - \boldsymbol{r}_2^*) = (\pi/6)U((1/2) - r_{12}^*)$ however other forms are possible, in particular the one proposed by Nordholm et al. [5]. In the latter case coarse-graining is taken over a reduced volume equal to $4\pi/3$ rather than $\pi/6$ and this would certainly alleviate the problem of physically unrealistic densities appearing in g_2. From their analysis of the homogeneous hard-sphere direct correlation function, Fischer and Heinbuch suggest that a simple linear combination of the functionals obtained from these two coarse-graining procedures may be advantageous. A study of this type is not undertaken here but could prove worthwhile in future work.

Diffusion

We now turn to a discussion of the results obtained from the MD simulations which are summarized in Table 4. We note that solvation forces were not calculated in these runs, however as a cross-check with the Monte Carlo simulations we did compute density profiles in a few cases and these were found to be in excellent agreement with the results shown in Figures 9 and 10.

The tracer diffusion coefficients computed using Equation (21) and the results given in Table 4 are plotted in Figure 12. The empirical correlation of Satterfield et al [21] is also shown in this figure and in this case we observe much better agreement between the simulation results and experiment. The molecular dynamics results are, however, generally lower for wall 2 and exhibit stronger fluctuations with pore size in comparison with the structureless model. We believe one of the major reasons for the systematically lower diffusion coefficients obtained here may be explained as follows. The experimental diffusion coefficients reported in [21] were obtained for a range of solutes of different size in a single porous medium (silica-alumina catalyst beads). The pore wall surface atoms or groups and their spacing were therefore of fixed size, designated approximately by σ_W, while the ratio σ_W/σ_1, where σ_1 is the characteristic size of the solute particle, decreased with increase in λ. The most important effect of lowering σ_W/σ_1 is a smoothing of the particle/pore wall potential energy surface with a consequent change of fluid structure and a reduction in the degree of backscattering of the fluid particles off the pore wall.

Table 4 System Characteristics and MD Simulation Results for Pores with Structured Walls (Wall 2)

[a]λ	[a]L^*	[b]N	[a]$N_1(10^{-3})$	[a]$N_1^R(10^{-3})$	T^*	[a]$\Omega_{1,1}^{(2)}(10^{-2})$	[c]$\Omega_{00}^{(2)}(10^{4})$
0.200	7.5	192	195	10	1.16	5.01(11)	10.3(2.2)
0.247	11.5	194	219	9	1.15	2.93(07)	5.24(86)
0.294	15.0	197	217	7	1.15	0.659(28)	1.78(33)
0.325	17.0	189	202	7	1.14	0.409(21)	0.70(35)
0.364	26.5	199	202	7	1.14	1.078(24)	1.38(38)
0.413	33.0	193	262	7	1.15	0.535(24)	0.41(31)
0.478	50.0	199	241	6	1.16	0.841(44)	0.62(22)
0.574	101.0	200	216	6	1.14	0.243(30)	1.08(36)

[a]As in Table 2.
[b]N is the number of particles used in a given simulation.
[c]$\Omega_{00}^{(2)}$ is the phenomenological coefficient calculated using Equation (20) and reduced by $\sigma\sqrt{\varepsilon m}$.
In each run, t^*_{max}, as defined in Table 2, was 6.0.

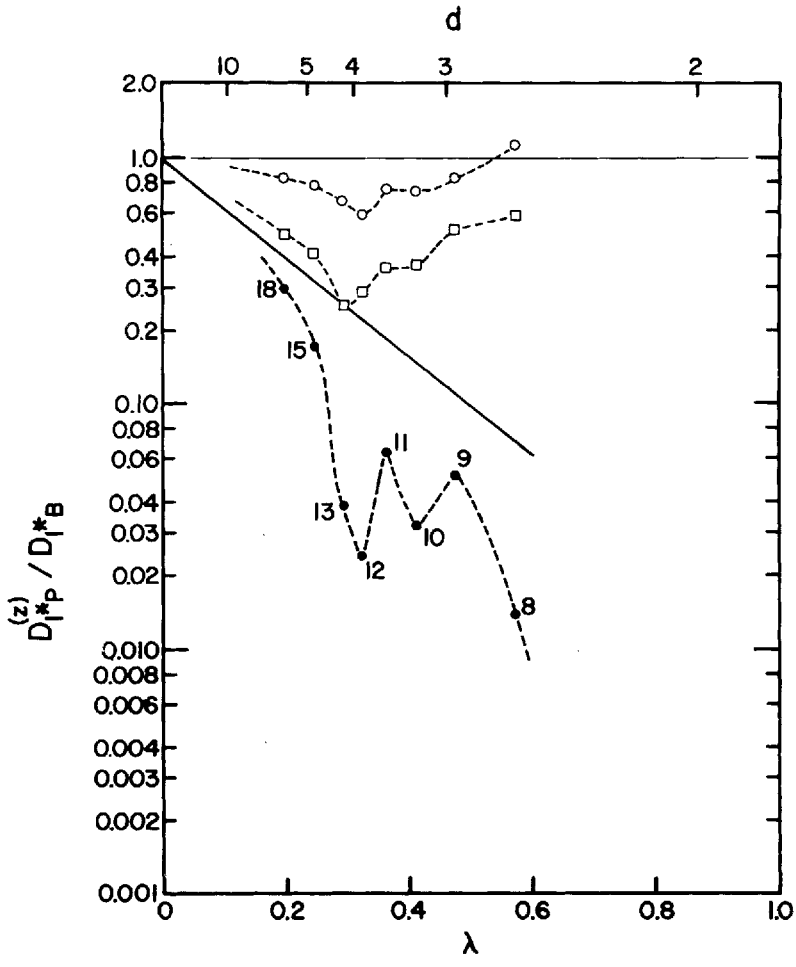

Figure 12 Reduced axial diffusion coefficient for the tracer as a function of λ in pores with wall 2. d as in Figure 3. – – ● – – MD simulation; – – □ – – Davis-Enskog kinetic theory (Fischer-Methfessel approximation); – – ⊙ – – Davis-Enskog kinetic theory (bulk fluid approximation); —— the empirical correlation of Satterfield et al [21]. The numbers next to the simulation points refer to the value of N_R in Equation (3).

Another way of viewing the severe reduction in $D^{(z)}_{i*P}$ is by way of arguments based on energy barriers. The very existence of finite sized surface atoms or groups is synonymous with the existence of repulsive energy barriers and localization of fluid particles in potential minima as shown in Figures 9 and 10. In our structured pore wall studies the fluid particle/pore wall energy barrier is approximately constant while in the systems investigated by Satterfield et al [21] and in similar studies conducted by Chantong and Massoth [22] the barriers involved decreased as the relative size of the nonadsorbing solute particle increased. (We note that the magnitude of the potential parameters which we have employed in Equations (1) and (2) place the systems we have studied in a nonadsorbing or weakly adsorbing class. As an indication of the

strength of the potential we may consider the magnitude of the potential minimum for argon in a carbon pore as cited by Heinbuch and Fischer [13]. For a pore of radius $R_P^* = 5$ they quote $\phi_{W,min}/kT = -10/T^*$ which is approximately a factor of two larger than the corresponding value for our structured system.)

The above comments do not preclude other reasons for the differences observed between simulation and experiment. In particular, our choice of surface lattice structure is an idealization more closely akin to crystalline media such as zeolites than amorphous porous media. The oscillations in $D_{1*P}^{(z)}$ shown in Figure 12 are in fact intimately related to the lattice structure of the wall. For the five smallest pores $N_R = 12$, 11, 10, 9, and 8, the average number of fluid particles per polygonal ring (one σ in pore length as shown in Figure 1 (b)) is approximately 5, 4, 3, 2, 1 respectively. The reason for the minimum in $D_{1*P}^{(z)}$ at $\lambda = 0.325$ ($N_R = 12$) is easily explained with reference to Figures 9 and 10. From Figure 9 (b), which corresponds to the profiles for particles in the pore window, we observe a very sharp peak in the density profile at $r = 0$. In contrast, inside the polygonal cage the density is strongly peaked at the pore wall and this peak is actually located at a distance 1σ from the center of the pore. Straightforward geometrical considerations show that of the five particles coordinating with one polygonal ring in this case, four are located at $r = 1\sigma$ inside the cage and one is located, on average, in the pore window. Although the particle in the pore window can move with comparative ease through the 1σ channel created by the four particles within the cage, the movement of the latter particles is highly restricted due to the presence of the window particle. With a reduction in N_R from 12 to 11 the window particle is eliminated and the potential barrier of mean force acting on the cage particles is reduced. The diffusion coefficient therefore increases as shown in Figure 12. As we move to the smaller pore with $N_R = 10$ the potential of mean force acting on the particles with a cage increases again and $D_{1*P}^{(z)}$ drops off. This is observed in Figure 9(a) where the window profile for $N_R = 10$ is seen to be significantly lower than for $N_R = 11$. A further decrease in the pore size however leads to a reduction in the number of particles per cage and the greater mobility of the particles is observed as an increase in the window profile as shown in Figure 9(a) for $N_R = 9$. The density profiles for $N_R = 9$ and 10 also suggest a two-dimensional mode of diffusion while in the larger pores, particles near the pore axis contribute to the diffusion process. In the smallest pore studied ($N_R = 8$) diffusion is pseudo-one-dimensional. The very large drop in the diffusion coefficient in this case is again related to a sharp rise in the potential of mean force since only one particle can fit into a cage. Although we do not present results for smaller pores, we did attempt to carry out MD simulations for $N_R = 7$ and 6. Unfortunately these simulations failed to provide adequate results for $D_{1*P}^{(z)}$ due largely to the persistence of long-time oscillations in the velocity autocorrelation function $\langle v_{1*z}(0)v_{1*z}(t) \rangle$. Our only conclusion at this point is that, in view of the particle numbers obtained from the Monte Carlo studies and the peak densities cited earlier for the profiles within the polygonal cage and in the pore window, the potential barrier for diffusion rapidly increases as λ approaches 1.0 and $D_{1*P}^{(z)}$ will continue its downward trend as shown in Figure 12.

In Figure 12 we also show results predicted by Davis' kinetic theory (Equations (28) and (30)) for the structured pore model using both the Fischer-Methfessel and bulk fluid approximations for g_2. These results were determined directly from the exact density profiles obtained in the simulations and numerical integration of Equations (28) and (30) was performed using the trapezoidal rule. The mesh size in the radial

direction was again 0.01 R_P^* and in view of the comparatively weak θ-dependence of the profiles found in the simulations the mesh increment $0.2\,\pi/N_R$ in this direction was retained. In the z-direction the mesh size 0.1 in the simulation profiles was considered to be too coarse and a finer grid with a 0.02 mesh increment was generated by interpolating the data using a cubic spline. The remaining details of the numerical integration were similar to those outlined in the analysis of the YBG equation.

The results shown in Figure 12 illustrate that Davis' theory predicts at most a fourfold drop in the diffusion coefficient within the pores if we assume that the Fisher-Methfessel approximation provides an adequate description of g_2. In the computations, however, we again found that the coarse-grained density $\bar{n}_P^*$ was frequently greater than the closest-packing density and the predicted values of $D_{l*P}^{(z)}$ in this case should therefore be considered as lower bounds on the possible results which could be obtained from Equations (28) and (30) with an accurate expression for g_2. On closer inspection of the assumptions implied in Equation (28) we find that there are two possible reasons for the relatively weak hindrance effects suggested by this theory.

Equation (28), and Enskog's theory upon which it is based, neglects dynamical correlations which can arise due to backscattering and caging in dense fluids and liquids. The importance of these correlations in the structured pore model is demonstrated in Figure 13 where we compare the tracer velocity autocorrelation functions for the structureless and structured pore walls at two values of λ. For the structureless systems the VACF decays monotonically in a manner similar to the simple exponential decay predicted by Enskog's theory. It is therefore not surprising that Equation (28) can quantitatively predict the behaviour of the tracer diffusion coefficient in this case. The VACF for the fluid particles in the structured pore, however, has a deep negative backscattering minimum which increases in magnitude as the pore size decreases. The plot for $\lambda = 0.478$ also shows incipient oscillations which, as mentioned earlier, are amplified in smaller pores due to caging of the fluid particles between the polygonal rings. These dynamical effects are the primary cause for the very low MD values for $D_{l*P}^{(z)}$ as compared with the predictions of Davis' theory.

The second reason Equation (28) underpredicts the extent of restricted diffusion is apparent when we compare this equation and Equation (30) with Equation (17). The diffusion coefficient $D_{l*M}^{(z)}$ in Equation (17) takes into account the direct influence of the pore wall on the dynamics of the pore fluid. Davis' theory does not contain this term although the indirect affect of the pore wall on the structure of the fluid is taken into consideration through the fluid particle pair correlation function and the density profile.

The relative importance of the diffusion coefficient $D_{l*M}^{(z)}$ in Equation (17) may be determined by comparing the magnitude of the terms $N\Omega_{oo}^{(z)}$ and $\Omega_{l*l*}^{(z)}$ since the latter coefficient is very nearly equal to $D_{l*P}^{(z)}$ for the pore fluid/structured wall systems considered here. Using the results given in Table 4 we find that for $\lambda < 0.4$, $D_{l*M}^{(z)}$ contributes between 20–40% to the overall pore diffusion coefficient $D_{l*P}^{(z)}$. For the two runs at $\lambda = 0.413$ ($N_R = 10$) and $\lambda = 0.478$ ($N_R = 9$) $D_{l*M}^{(z)}$ is nearly equal to $D_{l*P}^{(z)}$ and the reason for this is clear from the density profiles shown in Figures 9(a) and 10(a). The profiles in both of these cases are the only ones which possess a solitary peak at the pore wall while at the same time the fluid density on the pore axis is essentially zero. The mobility of the fluid particles is therefore largely controlled by interactions with the pore wall and interactions (or cross-correlations) between the fluid particles themselves are of minor importance. This is also illustrated in Figure

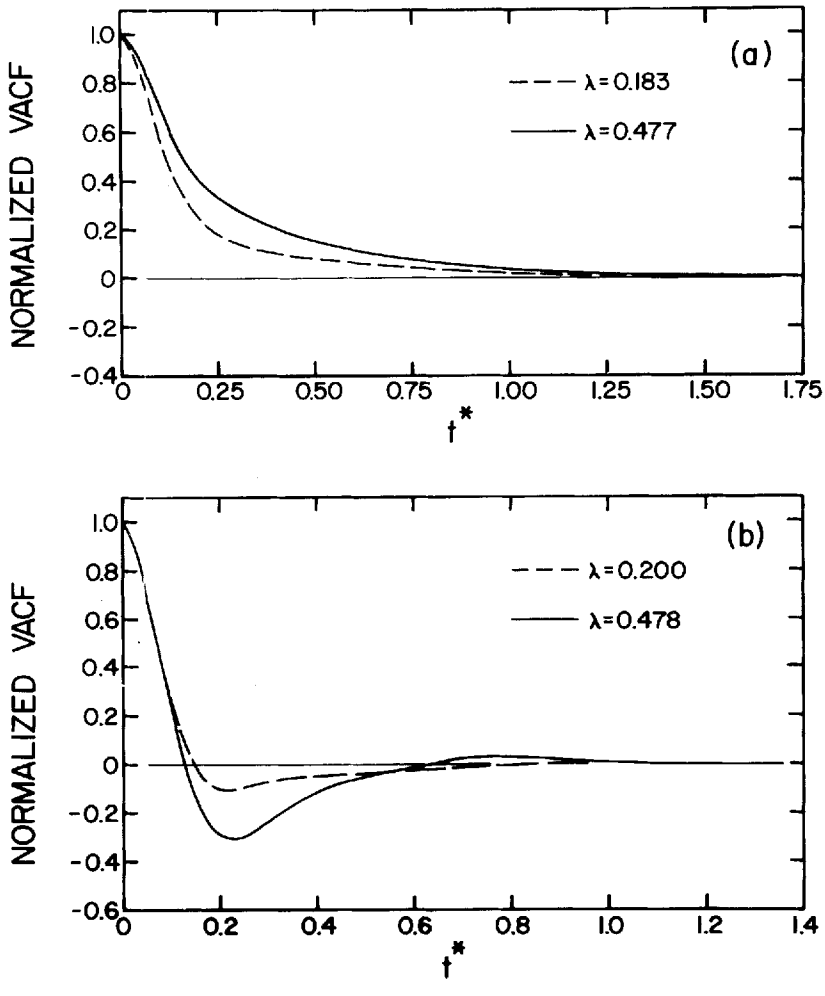

Figure 13 Normalized velocity autocorrelation functions corresponding to $\Omega^{(z)}_{1*}$ as a function of reduced time $t* = t\sqrt{\varepsilon/m\sigma^2}$. (a) The structureless pore wall; (b) The structured pore wall.

14 where we plot $D^{(z)}_{1*1}/D_{1*B}$ as a function of λ. The difficulty in trying to obtain reliable estimates for the small contribution $D^{(z)}_{1*1}$ makes to $D^{(z)}_{1*P}$ at $\lambda = 0.413$ and 0.478 is manifested by the extremely large error bars shown for this quantity. The value of $D^{(z)}_{1*1}/D_{1*B}$ at $\lambda = 0.413$ is in fact very poor and is only included here for completeness.

The result for $D^{(z)}_{1*1}/D_{1*B}$ at $\lambda = 0.574$ ($N_R = 8$) is of interest in that it is very close to the value of $D^{(z)}_{1*P}/D_{1*B}$ shown in Figure 12. In this case $D^{(z)}_{1*M}$ only contributes 10% to the pore diffusion coefficient which would appear to be contrary to expectations in view of the size of the pore. The reason for this however, has been alluded to earlier in the discussion of Figure 12. The number of particles per cage for $N_R = 8$ is approximately equal to 1.0 and, in order for diffusion to take place, any given particle

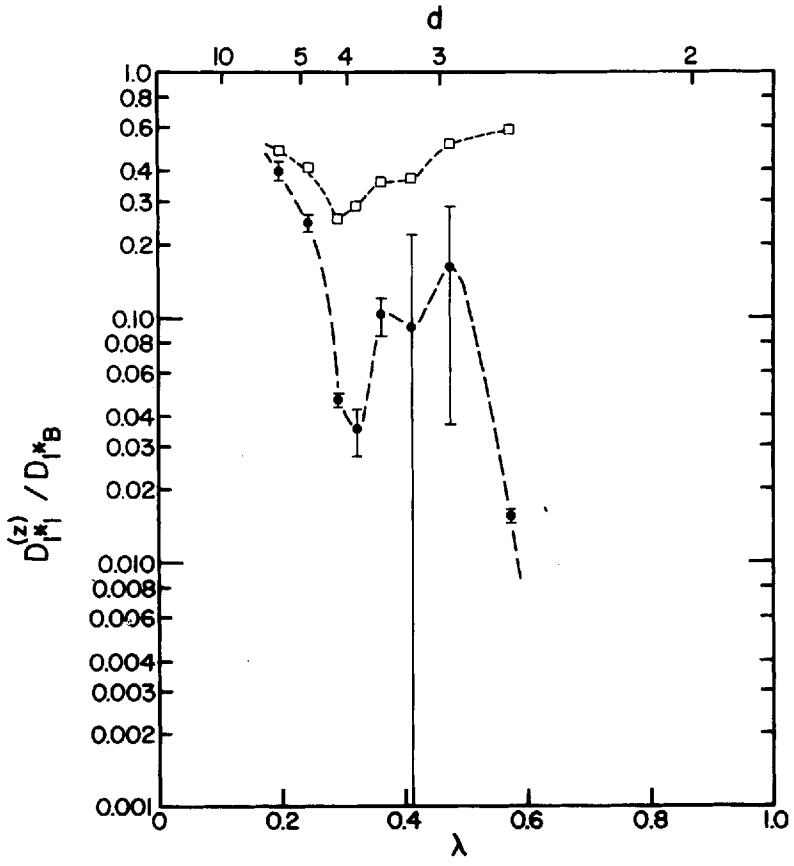

Figure 14 Reduced axial self-diffusion coefficient for the tracer as a function of λ for pore model 2. d as in Figure 3. – – ● – – MD simulation; – – □ – – Davis-Enskog kinetic theory (Fischer-Methfessel approximation).

must jump from its current position at a particular time into a neighboring cage which is, with high probability, already occupied. Cross-correlations between the fluid particles are therefore very strong and the denominator of Equation (19) should be large since we can write this as

$$N\Omega^{(z)}_{oo} - \Omega^{(z)}_{1*1*} = \frac{1}{N}\int_0^\infty dt \left\langle \sum_{\substack{j=1 \\ j\neq i}}^{N} v_{jz}(0) \sum_{\substack{i=1 \\ i\neq j}}^{N} v_{iz}(t) \right\rangle \tag{46}$$

The term in brackets is nothing more than the velocity cross-correlation function for the system.

To further emphasize the influence of wall friction on the mobility of the fluid particles in the pore we may consider coarse-grained local diffusion coefficients determined using Equations (22) and (23). In Table 5 we present results for the z and θ averaged local coefficients $\Omega^{(z)}_{1*1*}(\Delta V)$ and $\Omega^{(z)}_{oo}(\Delta V)$ for the two largest pores,

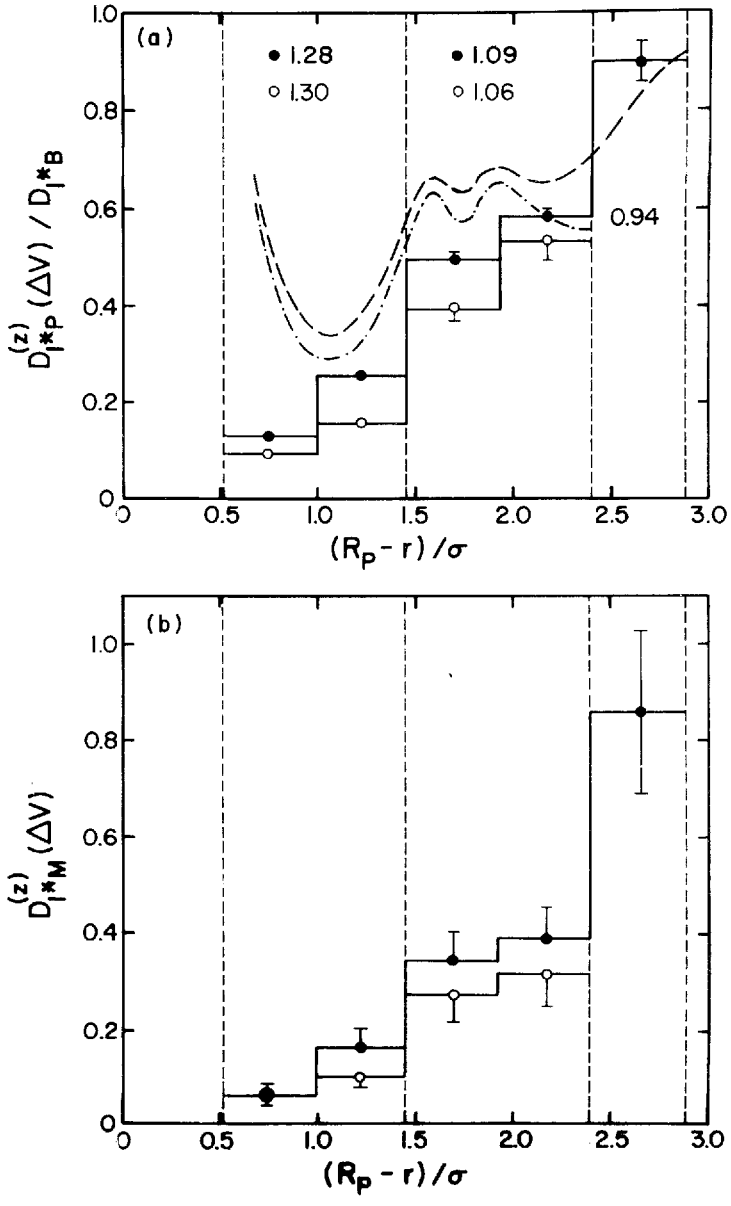

Figure 15 z and θ averaged local diffusion coefficients as a function of radial position from the wall in pore model 2. ΔV is the annular volume increment defined in Table 5. (a) Axial diffusion coefficient of the tracer reduced by D_{1*B}. —●— MD simulation results for $N_R = 18$ ($R_p^* = 2.879$); —○— MD simulation results for $N_R = 15$ ($R_p^* = 2.405$). - - - and -·-·- Theoretical results predicted by the Davis-Enskog kinetic theory (Fischer-Methfessel approximation) for $N_R = 18$ and 15 respectively. The numbers between the vertical dashed lines refer to the individual layer densities reduced by n_B^* in both pores. (b) Axial diffusion coefficient relative to the membrane reduced by $\sqrt{\varepsilon\sigma^2/m}$. All symbols are as in (a).

Table 5 Coarse-Grained Local Properties of the Fluid in Pores with Structured Walls.

[a]N_R	[b]$(R_P^* - r^*)_c$	[c]$\langle N(\Delta V)\rangle$	[d]$\Omega_{1*1*}^{(z)}(\Delta V)$ (10^2)	[d]$\Omega_{00}^{(z)}(\Delta V)$ (10^4)
	0.754	87.8(0.4)	0.736(50)	1.44(53)
	1.226	64.6(0.4)	0.895(42)	1.69(29)
15	1.698	29.2(0.3)	0.989(56)	2.11(38)
	2.170	12.4(0.2)	0.575(43)	1.05(23)
	0.754	75.7(0.2)	0.880(27)	1.19(54)
	1.226	54.8(0.2)	1.236(31)	2.44(57)
18	1.698	30.3(0.1)	1.334(36)	2.83(50)
	2.170	25.2(0.1)	1.313(40)	2.69(46)
	2.643	6.0(0.04)	0.479(26)	1.39(27)

[a]As in Table 3.
[b]Central location of the sublayers with the pore wall at the origin.
[c]$\langle N(\Delta V)\rangle$ is the ensemble averaged number of fluid particles in the volume element ΔV where $\Delta V/\sigma^3 = 2\pi L*\Delta r*^2(2i - 1)$ $(i = 1,2,\ldots)$ and $\Delta r* = 0.472$. The periodic half-lengths $L*$ are given in Table 4.
[d]$\Omega_{1*1*}^{(z)}(\Delta V)$ and $\Omega_{00}^{(z)}(\Delta V)$ are the local phenomenological coefficients calculated using Equations (22) and (23) and reduced by $\sigma\sqrt{\varepsilon/m}$.

$N_R = 15$ and 18, where ΔV corresponds to an incremental annular volume element approximately 0.5σ in width. The local values for $D_{1*P}^{(z)}(\Delta V)$ calculated using these results are plotted in Figure 15. The vertical dashed lines in this figure represent the boundaries of the individual fluid layers with the solid wall situated at the origin and the numbers recorded between the dashed lines in Figure 15(a) are the average layer densities reduced by n_B^*. It is clear from these results that the local particle mobility decreases sharply in the two layers nearest the pore wall. The pore size is seen to have only a marginal effect and we anticipate that in much larger pores the trends shown in Figure 15 will persist. The results shown in Figure 15(b) are of particular interest in that they represent the local fluid response to momentum slip in the axial direction of the pore. Near the wall, slip is negligible but increases rapidly as we move towards the center of the pore. In wide pores we expect $D_{1*M}^{(z)}(\Delta V)$ to approach very large values, if not infinity (perfect slip), in layers far from the wall.

The consequences of the omission of wall friction in Davis' theory are also demonstrated in Figure 15(a) where we plot the z and θ averaged local diffusion coefficients predicted by Equation (28) using the Fischer-Methfessel approximation for g_2. Even though $\bar{n}_P^*$ in Equation (26) can reach unrealistically high values in certain regions of the pore it would appear that Davis' theory can qualitatively predict the radial dependence of $D_{1*P}^{(z)}$ except at the pore wall where particle/pore wall axial momentum transfer is an overriding factor. This suggests that Equation (28) may provide a reasonable upper bound on the value of the self-diffusion coefficient $D_{1*1}^{(z)}$ within the pore as illustrated in Figure 14 however in order to provide a more complete formulation of the theory of transport in membranes it is clear that a detailed analysis of the dynamical properties of the fluid at the solid/fluid interface is needed.

Finally, we wish to consider a question raised in [25,26] concerning the magnitude of viscous slip in a realistic pore fluid/membrane system. A direct measure of this effect is given by the pore averaged coefficient $D_{1*M}^{(z)}$ and in order to compare our results for a Lennard-Jones liquid with those obtained earlier for a hard-sphere fluid we have plotted $D_{1*M}^{(z)}$, reduced by D_{1*K}, as a function of λ in Figure 16 where

$$D_{1*K} = \frac{2}{3}\sqrt{\frac{8kT}{\pi m_{1*}}}\, R_{PEFF}^*(1 - \lambda) \tag{35}$$

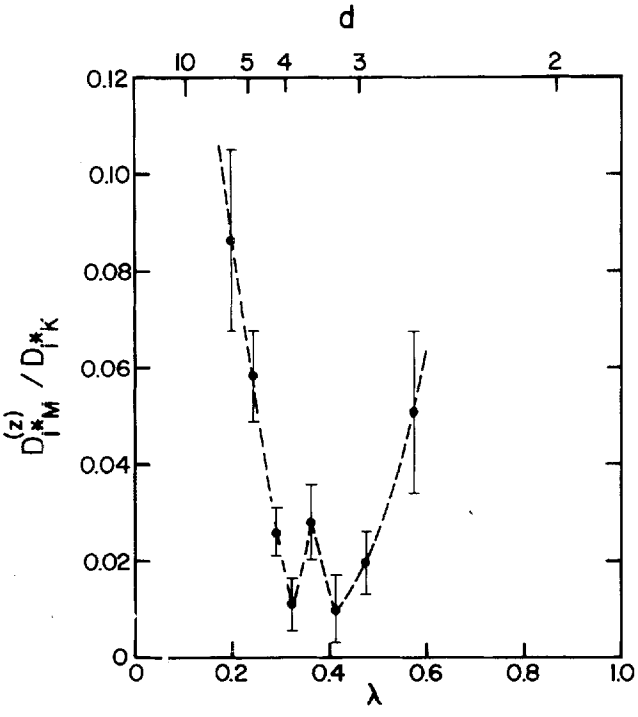

Figure 16 Reduced axial diffusion coefficient relative to the membrane vs. λ for pore model 2. --●-- MD simulation. D_{1*K} is the free molecule (Knudsen) diffusion coefficient (Equation (35)) and d is defined in Figure 3.

This term is the Knudsen diffusion coefficient corrected for size exclusion by the pore wall.

The results shown in Figure 16 are qualitatively similar to those reported in [25,26] for hard-sphere fluids subject to particle/pore wall diffuse scattering. The major differences lie in the magnitude of $D^{(z)}_{1*M}$and the deep minimum observed in the range $0.3 < \lambda < 0.5$. For $\lambda > 0.5$ the trend towards larger values of $D^{(z)}_{1*M}/D_{1*K}$ is in agreement with the hard-sphere results however the dramatic increase in $D^{(z)}_{1*M}/D_{1*K}$ towards smaller values of λ is quite different to the behaviour reported in [25] for a hard-sphere fluid at bulk density $n^*_B = 0.6$. The reason for this is briefly explained as follows. In [26] it was shown that $D^{(z)}_{1*M}$ is intimately related to the peak density of the fluid in contact with the pore wall and a similar relationship may be expected to hold for the systems under consideration here. Indeed, if we compare the trends in the magnitudes of the density peaks nearest the pore wall in figure 10 with the oscillatory behaviour of $D^{(z)}_{1*M}$ we observe that an inverse relationship does exist. The profiles within the polygonal cage are considered here since it is those particles which are localized on the adsorption sites (position 3 in Figure 2) which are primarily involved in axial momentum transfer with the surface atoms. If the trend shown in Figure 16 continues for $\lambda < 0.2$ then the viscous slip coefficient for a continuum Lennard-Jones fluid in contact with a simple cubic crystal of the same Lennard-Jones particles may

be obtained approximately by exptrapolating to $\lambda = 0$ to give 0.2. Although this value is lower than the hard-sphere result estimated for the system studied in [25] it does confirm our earlier conclusion that viscous slip exists for liquids. In light of the comparison made between shear flow and viscous slip in [26] we also suggest that slip flow should not be neglected as a viable mechanism for transport in microporous membranes.

4. SUMMARY AND CONCLUDING REMARKS

In this paper we have employed computer simulation techniques to determine the properties of a Lennard-Jones liquid in two model cylindrical pores. In the first model the fluid particle/pore wall interaction was described by a simple continuum potential function with scattering characterized by specular reflection. The choice of potential parameters provided results for the fluid properties which were comparable in magnitude to those reported earlier for hard-sphere fluids [25,26], and contrasts between both systems were found to be primarily due to differences in the structure of the fluid density peak at the pore wall. Due to its simplicity, the continuum model also permitted a detailed comparison with the Fischer-Methfessel [4] and bulk fluid [1,10] approximations to the YBG equation. The density profiles and solvation forces predicted by both approximations were in favorable agreement with the simulation results. Diffusion coefficients predicted by Davis' theory [23] were also found to agree well with simulation except in pores smaller that twice the size of the fluid particles. In this range of pore sizes a transition in fluid dimensionality would appear to preclude the applicability of three-dimensional theories of transport.

Although the continuum model provides a simple test case for current theories of micropore fluids, one of its major failings when coupled with specular scattering conditions is the physically unrealistic trend it portrays in the pore size dependence of the diffusion coefficient. In the second pore model investigated here, a square lattice of Lennard-Jones atoms was introduced into the solid surface of the cylindrical pore wall. The pore fluid diffusion coefficients obtained for this system differed by orders of magnitude from those determined using the continuum model and these results were also found to be in much better agreement with experimental data reported in the literature. The reasons for the sharp change in diffusion behaviour between the two models are (i) the lattice structure of the pore wall in the second model enhances long-range as well as short-range order of the micropore fluid and (ii) by introducing a non-continuum structure into the surface of the solid we provide a realistic mechanism for fluid particle/pore wall backscattering. In view of the highly structured density profiles obtained with the second model it is also not surprising that the pore averaged equilibrium properties of the fluid were significantly affected. In this case the partition coefficients were consistent with Gurvitsch's rule [40] and the solvation forces displayed an oscillatory behaviour which was qualitatively similar to that observed experimentally for slit-shaped cavities [14–16].

A comparison between the simulation results for the structured model and the Fischer-Methfessel [4] and bulk fluid [1,10] approximations to the YBG equaiton was also undertaken, and it was found that both methods provided reasonable estimates for the solvation force. In this case the general shape of the density profiles predicted by the method proposed by Fischer and Methfessel were qualitatively better, however physical inconsistencies arose due to overestimation of coarse-grained local densities

required in this approach. In an analysis of Davis' kinetic theory [23] we found that quantitative discrepancies in the predicted diffusion coefficients within structured pores were associated with an incomplete description of the dynamical properties of the fluid. In particular, the influence of particle/pore wall momentum transfer (friction) needs to be included in the theory.

One of the most important implications of the results presented here is that due care must be exercised when choosing a model particle/pore wall potential for a realistic system. When the pore wall surface atoms or groups and their spacing are small in size relative to the fluid particles, computations based on continuum potential models should provide a reliable representation of the structure of the fluid within the pore and at the solid/fluid interface. However, even for near-uniform surfaces, inelastic scattering of the fluid particles will usually dictate a diffuse reflection condition similar to that employed in [25,26] when dynamical studies are under consideration. If, on the other hand, the particle/pore wall potential displays significant site localization or repulsion barriers due to the commensurate size of the surface groups and fluid particles, then the detailed structure of the solid surface must be taken into account.

Acknowledgements

This research was supported by the National Science Foundation under grant CBT-8505246. The assistance of the University of Missouri-Rolla Computer Center is also gratefully acknowledged.

Appendix

The equilibrium properties for the bulk phase and pore fluid systems were determined using the GCEMC procedure described by Adams [42,43]. The slight modifications required to adapt this method to pore simulations at the same chemical potential as the bulk were similar to those discussed in [31]. The only differences were with regard to criteria associated with the potential energy functions, in particular the cut-off radius for interaction, R_c. The Lennard-Jones (12–16) interaction between the fluid particles in both the bulk and pore phases was truncated at $R_c = 3.3\sigma$. No cut-off was employed with the potential $\phi_{iW}^{(1)}$ for the continuum wall (Equation (1) in the main text). However, since this function could result in a large expenditure of CPU time if evaluated at each step during a simulation, we calcuated $\phi_{iW}^{(1)}$ independently and stored the results in a vector containing 5×10^3 elements spanning the range $0 \leqslant r \leqslant R_P$. A straightforward search routine with linear interpolation between elements was then incorporated into the simulation code to evaluate the particle/pore wall potential energy at any given value of r. The same procedure was employed in computing the force between a fluid particle and the structureless wall. The continuum interaction term in Equation (2) in the main text was calculated in the same manner although the cut-off $R_c = 3.3\sigma$ was imposed for interactions between a fluid particle and surface atoms of the set $\{S\}$.

The GCEMC simulations were conducted at a reduced temperature $T^* = 1.15$ and at a chemical potential $\mu = -10.954\,kT$. This value of μ corresponds to an argon-like Lennard-Jones fluid represented by Equation (4) in the paper with potential parameters $\varepsilon/k = 119.8$K, $\sigma = 3.405$Å and atomic mass $m = 6.633 \times 10^{-23}$g. In the bulk fluid simulations with a fundamental cell of volume $V = 512\,\sigma^3$, this chemi-

cal potential is equivalent to $B = 3.3$ in the GCEMC algorithm proposed by Adams [43]. The Markov chains generated in the Monte Carlo studies were composed of 2.5×10^6 compound events for the bulk phase (each compound event consists of a trial move and an attempted addition or removal of a particle) and between $5 \times 10^6 - 7 \times 10^6$ compound events for the pore simulations. The simulations were initiated with fundamental cells devoid of fluid particles and the first 0.5×10^6 events (bulk phase) and $1 \times 10^6 - 1.5 \times 10^6$ events (pore phase) were discarded. Equilibrium ensemble averages were obtained over the latter part of the chains. Statistical uncertainties in the calculated properties were determined from at least 40 partial averages sampled over the equilibrium ensemble of a given simulation run. Long-range corrections are not included in any of the results reported here.

In the molecular dynamics simulations Newton's equations of motion for the individual fluid particles were numerically integrated using Gear's fifth order predictor-corrector method [44,45] with a time step equal to $0.005\sigma\sqrt{m/\varepsilon}$ in all runs. Interactions with the pore wall were treated in a manner similar to that outlined above in the Monte Carlo simulations. For pores larger than twice the size of the Lennard-Jones particles the initial configurations were generated by randomly inserting the number of particles prescribed by the GCEMC results. In pores smaller than $1/\lambda = 2$ the particles were initially placed in a uniform string along the pore axis. Initial velocities were randomly assigned from the Maxwell-Boltzmann distribution and subsequently scaled to give zero mass average velocity components in the coordinate frame of the system. During the equilibration stage this scaling procedure as well as scaling of the fluid kinetic energy was repeated every 50 time steps. The length of the trajectory generated for any individual pore simulation in the equilibrium NVE ensemble was between 0.72×10^5 and 4.25×10^5 time steps and the properties of the fluid were evaluated from appropriate time averages. A bulk fluid simulation was also carried out on a periodic cubic cell containing 200 particles in order to determine the tracer diffusion coefficient D_{1*B}. The number of equilibrated time steps used in this case was 10^5. Statistical uncertainties in the bulk and pore fluid properties were computed from partial averages obtained over independent increments of $4 \times 10^3 - 5 \times 10^3$ time steps along the individual trajectories.

All of the computations reported here were carried out on an FPS-164 computer at the University of Missouri-Rolla.

References

[1] J. Fischer, "A Fluid in Contact with a Wall. The Percus-Yevick versus the Superposition Approximation", *Mol. Phys.*, **33,** 75 (1977).

[2] W. van Megen and I.K. Snook, "Structure and Solvation Forces Between Solid Bodies", *J. Chem. Soc. Faraday Trans. II* **75,** 1095 (1979).

[3] J.E. Lane and T.H. Spurling, "Forces Between Adsorbing Walls: Monte Carlo Calculations", *Chem. Phys. Lett.*, **67** 107 (1979).

[4] J. Fischer and M. Methfessel, "Born-Green-Yvon Approach to the Local Densities of a Fluid at Interfaces", *Phys. Rev. A.*, **22** 2836 (1980).

[5] S. Nordholm, M. Johnson, and B.C. Freasier, "Generalized van der Waals Theory. III The Prediction of Hard-Sphere Structure", *Aust. J. Chem.*, **33,** 2139 (1980).

[6] I.K. Snook and W. van Megen, "Solvation Forces in Simple Dense Fluids. I. ", *J. Chem. Phys.*, **72,** 2907 (1980).

[7] W. van Megen and I.K. Snook, "Solvation Forces in Simple Dense Fluids. II. Effect of Chemical Potential", *J. Chem. Phys.*, **74,** 1409 (1981).

[8] D. Nicholson and N.G. Parsonage, Computer Simulation and the Statistical Mechanics of Adsorption, Academic Press, N. Y. (1982).
[9] B.C. Freasier and S. Nordholm, "A General van der Waals Model for Solvation Forces Between Solute Particles in A Colloidal Suspension", *J. Chem. Phys.*, **79,** 4431 (1983).
[10] V. Ya. Antonchenko, V.V. Ilyin, N.N. Makovsky, A.N. Pavlov, and V.P. Sokhan, "On the Nature of Disjoining Pressure Oscillations in Fluid Films", *Mol. Phys.*, **52,** 345 (1984).
[11] J.J. Magda, M. Tirrell, and H.T. Davis, "Molecular Dynamics of Narrow, Liquid-Filled Pores", *J. Chem. Phys.*, **83,** 1888 (1985).
[12] B.K. Peterson and K.E. Gubbins, "Phase Transitions in a Cylindrical Pore. Grand Canonical Monte Carlo, Mean Field Theory and the Kelvin Equation", *Mol. Phys.*, **62,** 215 (1987).
[13] U. Heinbuch and J. Fischer, "On the Application of Widom's Test Particle Method to Homogeneous and Inhomogeneous Fluids", *Mol. Sim.*, **1,** 109 (1987).
[14] R.G. Horn and J.N. Israelachvili, "Direct Measurement of Structural Forces Between Two Surfaces in a Nonpolar Liquid", *J. Chem. Phys.*, **75,** 1400 (1981).
[15] R.M. Pashley and J.N. Israelachvili, "Molecular Layering of Water in Thin Films Between Mica Surfaces and its Relation to Hydration Forces", *J. Colloid Interface Sci.*, **101,** 511 (1984).
[16] H.K. Christenson, "Experimental Measurements of Solvation Forces in Nonpolar Liquids", *J. Chem. Phys.*, **78,** 6906 (1983).
[17] W.L. Haberman and R.M. Sayre, "Motion of Rigid and Fluid Spheres in Stationery and Moving Liquids Inside Cylindrical Tubes", David Taylor Model Basin Report No. 1143, U. S. Navy, Washington, D. C. (1958).
[18] J.L. Anderson and J.A. Quinn, "Restricted Transport in Small Pores. A Model for Steric Exclusion and Hindered Particle Motion", *Biophys. J.*, **14,** 130 (1974).
[19] H. Brenner and L.J. Gaydos, "This Constrained Brownian Movement of Spherical Particles in Cylindrical Pores of Comparable Radius. Models of the Diffusive and Convective Transport of Solute Molecules in Membranes and Porous Media.", *J. Colloid Interface Sci.*, **58,** 312 (1977).
[20] R.E. Beck and J.S. Schultz, "Hindrance of Solute Diffusion within Membranes as Measured with Microporous Membranes of Known Pore Geometry", *Biochim. Biophys. ACTA*, **255,** 273 (1972).
[21] C.N. Satterfield, C.K. Colton, and W.H. Pitcher Jr., "Restricted Diffusion in Liquids within Fine Pores", *AIChE Journal*, **19** 628 (1973).
[22] A. Chantong and F.E. Massoth, "Restrictive Diffusion in Aluminas", *AIChE Journal*, **29** 725 (1983).
[23] H.T. Davis, "Kinetic Theory of Inhomogeneous Fluid: Tracer Diffusion", *J. Chem. Phys.*, **86,** 1474 (1987).
[24] T.K. Vanderlick and H.T. Davis, "Self-Diffusion in Fluids in Microporous Solids", *J. Chem. Phys.*, **87,** 1791 (1987).
[25] S.-H. Suh and J.M.D. MacElroy, "Molecular Dynamics Simulation of Hindered Diffusion in microcapillaries", *Mol. Phys.*, **58,** 445 (1986).
[26] J.M.D. MacElroy and S.-H. Suh, "Computer Simulation of Moderately Dense Hard-Sphere Fluids and Mixtures in Microcapillaries", *Mol. Phys.*, **60,** 475 (1987).
[27] D. Nicholson, "Molecular Theory of Adsorption in Pore Spaces. Part 1. Isotherms and Simple Lattice Models", *J. Chem. Soc. Faraday Trans. I*, **71,** 238 (1975).
[28] F.A. Putnam and T. Fort Jr., "Physical Adsorption on Patchwise Heterogeneous Surfaces. 2. Virial Coefficient Theory Analysis of Krypton Adsorption on Graphitized Carbon Black", *J. Phys. Chem.*, **81,** 2164 (1977).
[29] J. Karger, H. Pfeifer, M. Rauscher, and A. Walter, "Self-Diffusion of n-Paraffins in NaX Zeolite", *J. Chem. Soc. Faraday Trans. I*, **76,** 717 (1980).
[30] F.F. Abraham, "The Interfacial Density Profile of a Lennard-Jones Fluid in Contact with a (100) Lennard-Jones Wall and its Relationship to Idealized Fluid/Wall Systems: A Monte Carlo Simulation", *J. Chem. Phys.*, **68,** 3713 (1978).
[31] J.M.D. MacElroy and S.-H. Suh, "Concentration and Non-Continuum Effects in Size-Exclusion Partitioning", *AIChE Symp. Ser.*, **82,** No. 248, 133 (1986).
[32] E.A. Mason and L.A. Viehland, "Statistical-Mechanical Theory of Membrane Transport for Multicomponent Systems: Passive Transport Through Open Membranes", *J. Chem. Phys.*, **68,** 3562 (1978).
[33] J.H. Irving and J.G. Kirkwood, "The Statistical-Mechanical Theory of Transport Processes. IV. The Equations of Hydrodynamics", *J. Chem. Phys.*, **18,** 817 (1950).
[34] J.G. Kirkwood, "Statistical Mechanics of Fluid Mixtures", *J. Chem. Phys.*, **3,** 300 (1935).
[35] T.M. Reed and K.E. Gubbins, Applied Statistical Mechanics, McGraw-Hill Book Co., N. Y. (1973)
[36] J.L. Lebowitz and J.K. Percus, "Kinetic Equations and Density Expansions: Exactly Solvable One-Dimensional Systems", *Phys. Rev.*, **155,** 122 (1967).

[37] B.J. Alder, D.M. Gass, and T.E. Wainwright, "Studies in Molecular Dynamics. VIII. The Transport Coefficients for a Hard-Sphere Fluid", *J. Chem. Phys.*, **53,** 3813 (1970).
[38] A.J. Easteal, L.A. Woolf, and D.L. Jolly, "Self-Diffusion in a Dense Hard-Sphere Fluid: A Molecular Dynamics Simulation", *Physica*, **121A,** 286 (1983).
[39] I.–A. Park and J.M.D. MacElroy, "Simulation of a Hard-Sphere Fluid in Bicontinuous Random Media", *Mol. Sim.* (in press).
[40] M.J. Jaycock and G.D. Parfitt, Chemistry of Interfaces, J. Wiley & Sons, N. Y. (1981).
[41] J. Fischer and U. Heinbuch, "Relationship Between Free Energy Density Functional, Born-Green-Yvon, and Potential Distribution Approaches for Inhomogeneous Fluids", *J. Chem. Phys.*, **88,** 1909 (1988).
[42] D.J. Adams, "Chemical Potential of Hard-Sphere Fluids by Monte Carlo Methods", *Mol. Phys.*, **28,** 1241 (1974).
[43] D.J. Adams, "Grand Canonical Ensemble Monte Carlo for a Lennard-Jones Fluid", *Mol. Phys.*, **29,** 307 (1975).
[44] C.W. Gear, Numerical Initial Value Problems in Ordinary Differential Equations, Prentice-Hall, Englewood Cliffs (1971).
[45] J.M. Haile, A Primer on the Computer Simulation of Atomic Fluids by Molecular Dynamics, Clemson University, Clemson (1980).